Final Technical Report

Grant No. FA9550-13-1-0163

(YIP) Elucidating the Wavelength Dependence of Phonon Scattering in Nanoparticle-Matrix Composites using Phonon Spectroscopy

Robert Wang
Arizona State University
School for Engineering of Matter, Transport and Energy
rywang@asu.edu

June 30, 2016

Project Dates: March 27, 2013 – March 31, 2016

Abstract

This project examined thermal transport and phonon transport in three types of nanoparticle-matrix composites: (i) semiconductor nanoparticles randomly distributed within a semiconductor matrix, (ii) semiconductor nanoparticles embedded in molecular matrices of varying composition, and (iii) nanoparticles periodically-arranged inside of a molecular matrix. This project specifically focused on colloidal nanocrystals (NCs), which are a type of nanoparticle that consists of an inorganic crystalline core with ligands bound to the surface. Solution-phase syntheses enable the precision control of size, shape, and composition of these colloidal NCs.

Nanoparticle-in-matrix composites are a common motif among many nanoscience applications and are of particular interest to the thermal sciences community. To explore this morphological theme, we created crystalline inorganic composites with nanoparticle volume fractions ranging from 0 to ~100%. We synthesized these composites by mixing colloidal CdSe NCs and In_2Se_3 metal chalcogenide complex (MCC) precursor in the solution-phase, and then thermally transforming the MCC precursor into a crystalline In_2Se_3 matrix. We found rich structural and chemical interactions between the CdSe NCs and the In_2Se_3 matrix, including alterations in In_2Se_3 grain size and orientation as well as the formation of a ternary phase, $CdIn_2Se_4$. With the exception of the ~100% CdSe samples, the thermal conductivities of these nanocomposites are insensitive to CdSe volume fraction and are ~0.3 W/m-K in all cases. We attribute this insensitivity to competing effects that arise from structural morphology changes during composite formation. These thermal conductivities are remarkably low for inorganic crystalline materials and are comparable to amorphous polymers.

We also systematically studied the effect of surface chemistry on thermal transport in NC solids. Using PbS NCs as a model system, we varied ligand binding group (thiol, amine, and atomic halides), ligand length (ethanedithiol, butanedithiol, hexanedithiol, and octanedithiol), and NC diameter (3.3-8.2 nm). Our experiments revealed several findings: (i) The ligand choice can vary the NC solid thermal conductivity by up to a factor of 2.5. (ii) The ligand binding strength to the NC core does not significantly impact thermal conductivity. (iii) Reducing the ligand length can decrease the interparticle distance, which increases thermal conductivity. (iv) Increasing the NC diameter increases thermal conductivity. (v) The effect of surface chemistry can exceed the effect of NC diameter and becomes more pronounced as NC diameter decreases. By combining these trends, we demonstrated that the thermal conductivity of NC solids can be varied by an overall factor of 4, from ~ 0.1-0.4 W/m-K. We complemented these findings with effective medium approximation modeling and identified thermal transport in the ligand matrix as the rate-limiter for thermal transport. Overall, we concluded that future efforts to increase thermal conductivity in NC solids should focus on the ligand-ligand interface between neighboring NCs.

Colloidal NCs can self-assemble into periodic arrays known as superlattices due to van der Waals interactions between their ligands. This periodic structure makes superlattices promising for phononic crystal applications. To explore this potential, we used plane wave expansion methods to model the phonon band structure. We found that the nanoscale periodicity of these superlattices yields phononic band gaps with very high center frequencies on the order of 10^2 GHz. We also found that the large acoustic contrast between the hard NC cores and the soft ligand matrix lead to very large phononic band gap widths on the order of 10^1 GHz. We systematically varied NC core diameter, d, NC core elastic modulus, $E_{NC\ Core}$, interparticle distance (i.e. ligand length), L, and ligand elastic modulus, E_{ligand}, and reported on the corresponding effects on the phonon band structure. Our modeling shows that the band gap center frequency increases as d and L are decreased, or as $E_{NC\ Core}$ and E_{ligand} are increased. The band gap width behaves non-monotonically with d, L, $E_{NC\ Core}$, and E_{ligand}, and intercoupling of these variables can eliminate the band gap. Lastly, we observe multiple phononic band gaps in many superlattices and find a correlation between an increase in the number of band gaps and increases in d and $E_{NC\ Core}$. We find that increases in the property mismatch between phononic crystal components (i.e. d/L and $E_{NC\ Core}$ / E_{ligand}) flattens the phonon branches and are a key driver in increasing the number of phononic band gaps. Our predicted phononic band gap center frequencies and widths far exceed those in current experimental demonstrations of 3-dimensional phononic crystals. This suggests that colloidal NC superlattices are promising candidates for use in high frequency phononic crystal applications.

1.0. Solution-Phase Synthesis and Thermal Conductivity of Nanostructured CdSe, In_2Se_3, and Composites Thereof

1.1. Introduction

Nanoparticle composites are a morphological theme spanning applications in thermoelectrics,[1-7] thermal storage,[8, 9] optoelectronics,[10, 11] memory,[12, 13] and smart windows.[14, 15] Solution phase processes are a promising fabrication route to such composites because they utilize mild temperatures, moderate pressures, and inexpensive equipment, which generally lead to cost reductions. In addition, solution-phase processes provide a modular route wherein pre-synthesized colloidal nanostructures and matrices can be mixed in the solution-phase and then converted into a solid-phase nanocomposite. This approach has been commonly used to embed colloidal nanocrystals into polymers,[9, 16, 17] oxides,[18-20] semiconductors,[21, 22] and metals.[8] Embedding colloidal nanocrystals into polymer matrices is generally straightforward because both of these materials are commonly soluble in a variety of solvents. On the other hand, inorganic matrices such as oxides, semiconductors, and metals are generally insoluble. This hurdle can be circumvented by identifying a soluble matrix precursor that can be mixed with colloidal nanocrystals and then converted into a solid inorganic matrix afterwards.

Metal-chalcogenide complexes (MCCs) have been demonstrated to be soluble precursors for a broad range of metal-chalcogenide materials such as tin, indium, antimony, germanium, gallium, mercury, copper, and zinc chalcogenides.[21, 23-26] These MCCs can also be used to replace the conventional organic ligands that passivate the surface of colloidal nanocrystals.[21, 22] MCCs used in this manner fall under the growing class of inorganic ligands for colloidal nanocrystals.[27] This class includes MCCs,[21] metal-free chalcogenides,[28] polyoxometallates,[20] halide, pseudohalide and halometallates.[29] The use of these inorganic ligands as led to greatly improved charge transport mobilities in colloidal nanocrystal materials on the order of 10^1 $cm^2/V\text{-}s$.[29-34] Promisingly, very recent work using CdSe nanocrystals functionalized with cadmium chalcogenidometallates has led to record mobility values on the order of 10^2 $cm^2/V\text{-}s$ and are within a factor of ~2 relative to single-crystal mobilities.[35] This running theme of inorganic ligands has led to works on colloidal nanocrystal routes to transistors and integrated circuits,[33, 36] photovoltaics,[37] smart windows,[14] and thermoelectrics.[31, 38-42]

One attractive trait of colloidal nanocrystals with MCC ligands is that by annealing them, the MCC ligands can be transformed into an ultrathin metal-chalcogenide layer between the nanocrystals,[21, 22, 34, 42, 43] thereby creating nanocomposites with an ~100% nanoparticle volume fraction. In addition, the large variety of colloidal nanocrystal and MCC choices enables excellent control over nanocomposite parameters such as nanoparticle size and composition as well as matrix composition.

Inspired by this approach to nanocomposite fabrication, we explore the use of this chemistry to control an additional and important nanocomposite variable, that of nanoparticle volume fraction. By varying the colloidal nanocrystal – MCC precursor ratio in solution prior to nanocomposite formation, we create composites with nanoparticle volume fractions ranging from 0 to ~100%. Although such control over nanoparticle volume fraction has been previously demonstrated, few characterization details were reported.[21] In this work, we combine CdSe nanocrystals with varying amounts of In_2Se_3 MCC precursor and then characterize the resulting composites with x-ray diffraction (XRD), transmission electron microscopy (TEM), scanning electron microscopy (SEM), Rutherford backscattering spectroscopy (RBS), particle-induced x-ray emission (PIXE), and energy dispersive x-ray spectroscopy (EDX). This work complements earlier works on CdSe nanocrystals with In_2Se_3 MCCs that focused on very high nanocrystal volume fractions, but did not otherwise explore the dimension of nanoparticle volume fraction.[34, 44]

The structural motif of nanoparticles embedded in a crystalline matrix is a common theme in the thermal science community.[1-5, 7, 45, 46] In particular, it is well known that matrix-embedded

nanoparticles promote broadband scattering of phonons, which correspondingly leads to low thermal conductivities. This is particularly important for thermoelectric applications wherein reduced thermal conductivities lead to large improvements in energy conversion efficiency.[1-5, 7] This paper's solution-phase synthesis approach contrasts with many of the recent materials processes used to create nanostructured thermoelectrics such as molecular beam epitaxy,[5] ball-milling/hot-pressing,[47, 48] melt-processing,[7] and melt-processing/power-processing/spark-plasma-sintering.[1] In particular, the use of colloidal nanocrystals enables precise size control over the nanoparticle inclusions that is not possible by these other processing approaches. Furthermore, recent computational work suggests that the best nanoparticle size distribution for minimum thermal conductivity is neither a narrowly monodisperse or broadly polydisperse diameter distribution.[49] Instead the optimal size distribution consists of a mixture of several different monodisperse diameters.[49] Composites such as this could be achieved by mixing together colloidal nanocrystals of different diameters. It should also be noted that a recent cost-analysis on thermoelectric materials and manufacturing suggests that solution-phase processing could lead to significant cost improvements relative to typical thermoelectric materials processing. [50]

Due to the importance of this nanoparticle-in-matrix structural motif to the thermal science community, we measured the thermal conductivity of our nanoparticle-in-matrix composites as a function of nanoparticle volume fraction. We find that the thermal conductivity of the CdSe – In_2Se_3 composites is very low over the entire nanoparticle volume fraction range. The average thermal conductivity of the ~100% CdSe composites is 0.53 W/m-K, which is 17 times lower than bulk single crystal CdSe.[51, 52] The average thermal conductivity of the 100% In_2Se_3 composites is 0.32 W/m-K, which is 3 times lower than other literature results on polycrystalline In_2Se_3.[53] With the exception of the ~100% CdSe sample, the thermal conductivities of these nanocomposites are insensitive to CdSe volume fraction. We believe this insensitivity is due to competing effects that both increase and decrease the composite's thermal conductivity. Many of these competing effects arise from changes in structural morphology as the composites are formed (i.e. ternary phase formation, grain orientation and size changes) and will be discussed below.

1.2. Experimental Section

1.2.1. Nanocomposite Synthesis

The nanocomposites were prepared using a four-step approach: (i) synthesis of colloidal CdSe nanocrystals (ii) functionalization of the CdSe nanocrystal surface with In_2Se_3 MCC precursor, (iii) controllably adding additional In_2Se_3 MCC precursor, and (iv) decomposing the In_2Se_3 MCC precursor into a polycrystalline In_2Se_3 matrix that encapsulates the nanocrystals.

The In_2Se_3 MCC was made by reacting In_2Se_3 with Se and N_2H_4 to form $(N_2H_4)_2(N_2H_5)_2In_2Se_4$.[23] We confirmed the decomposition conditions for transforming this precursor into In_2Se_3 using thermogravimetric analysis. We heated the precursor to 350 °C, applied a 30 minute isotherm, and then continued to heat the precursor to 450 °C (Figure 1.1). The lack of mass loss after the 350 °C isotherm indicates that the thermal decomposition process was complete. Composites consisting of 100% In_2Se_3 were made by directly using this precursor.

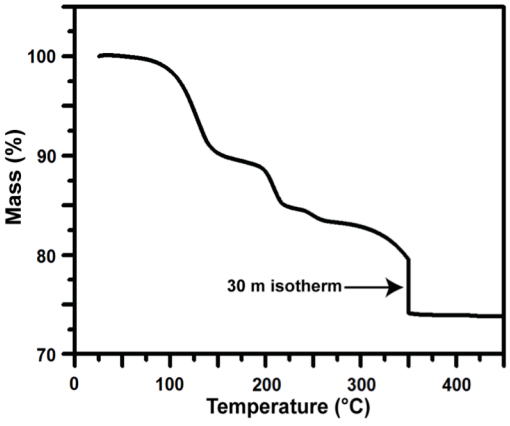

Figure 1.1. Thermogravimetric analysis of the In_2Se_3 MCC, $(N_2H_4)_2(N_2H_5)_2In_2Se_4$. The temperature ramp rate was 2 °C/min and a 30-minute isotherm was applied at 350 °C.

Wurtzite phase CdSe nanocrystals were synthesized by the hot injection method reported by Qu *et al.*[54]. As synthesized the CdSe nanocrystal surface is passivated by a combination of stearic acid (SA) and trioctylphosphine oxide (TOPO) ligands. These organic ligands were exchanged with the In_2Se_3

MCC precursor using the phase transfer process described by Kovalenko *et al.*[21] Two immiscible solutions, CdSe nanocrystals in hexane and MCC precursor in hydrazine, were combined and stirred for several hours. During this process, the hydrazine phase changed from colorless to dark, indicating the presence of CdSe nanocrystals functionalized with In_2Se_3 MCC precursor. The CdSe nanocrystals were then precipitated several times to separate them from unbound In_2Se_3 MCC precursor. Nanocomposites that are ~100% CdSe were made by directly using this nanocrystal solution. Nanocomposites with lower nanoparticle volume fractions were made by re-introducing appropriate amounts of In_2Se_3 MCC precursor back into the CdSe nanocrystal solution.

The elemental composition of the composite was determined by a combination of RBS and PIXE. Since the CdSe nanocrystals and In_2Se_3 matrix in the composite reacted to form a third phase, $CdIn_2Se_4$, this elemental composition information cannot definitively determine the CdSe volume fraction in the composite (see XRD discussion in Section 3.1). Consequently we identify our composites by their In_2:Cd ratio. In the absence of $CdIn_2Se_4$ formation, a 40:60 ratio implies a composite that is 40 mol% In_2Se_3 and 60 mol% CdSe. Since the CdSe nanocrystal surface was functionalized with In_2Se_3 MCC precursor, the ~100% CdSe composites have trace amounts of In.

1.2.2. Thermal Conductivity Measurements

Thermal conductivity measurements were conducted using the differential 3ω method.[55-57] Nanocomposite samples were prepared by spin-coating the CdSe nanocrystal – In_2Se_3 MCC precursor solution onto silicon substrates and then thermally decomposing the In_2Se_3 MCC precursor at 350 °C for 30 minutes. The sample film thickness generally ranged from 50 – 130 nm. A 50 nm Al_2O_3 dielectric layer was first deposited on top of the nanocomposite film using electron beam evaporation. 150 nm thick Al 3ω lines were then patterned on top of the dielectric layer using standard lithographic techniques. Line dimensions were generally 500 – 1000 μm long and 5 – 6 μm wide, however line widths up to 20 μm were occasionally used. A Keithley 6221 was used as the current source and a Stanford Research Systems SR830 lock-in amplifier was used to measure the 1st and 3rd harmonics of the voltage signal. The temperature coefficient of resistance of the 3ω lines were measured using a custom-built temperature-controlled sample stage. The nanocomposite film thickness was measured by profilometry prior to deposition of the 50 nm Al_2O_3 dielectric layer.

Since the 3ω method measures the combined thermal response of the dielectric layer, nanocomposite film, and substrate, identical reference samples consisting of only the dielectric layer and substrate were prepared simultaneously with the nanocomposite samples. Subtracting the thermal response of the reference sample from the measurement samples enables the nanocomposite thermal conductance to be isolated.

1.3. Results and discussion

1.3.1. Nanocomposite Structure

The TEM images (Figure 1.2) reveal that the nanocomposite consists of randomly dispersed nanoparticles embedded in a matrix. While the general nanoparticle shape is retained throughout the composite formation, we do observe a slight increase in nanoparticle size after composite formation. The average diameter of the as-synthesized CdSe nanocrystals is 8.2 nm (Figure 1.2a,e) whereas the average nanoparticle diameter in the 50:50 composite is 9.0 nm (Figure 1.2c,e). We believe this slight growth in nanoparticle size is due to the formation of $CdIn_2Se_4$ at the interface between the CdSe nanocrystal and the In_2Se_3 matrix (see XRD discussion). In the absence of CdSe nanocrystals, the formation of relatively large In_2Se_3 grains is observed (38 ± 12 nm, Figure 1.2d).

The SEM images (Figure 1.3) show that mass loss and densification during thermal conversion of the MCC precursor into In_2Se_3 lead to mesoporosity in the nanocomposites. This mesoporosity

was also evident when comparing film thicknesses measured via RBS and profilometry; profilometry thicknesses were approximately 20% greater than thicknesses determined by RBS, which assume fully dense films. Structural features on the order of 10^1 and 10^2 nm in size are visible in the SEM images of 100% In_2Se_3 (Figure 1.3d). By comparison with the TEM images, we believe the 10^1 nm-scale features correspond to the In_2Se_3 grains whereas the 10^2 nm-scale features correspond to defects formed during thermal decomposition of the MCC precursor. Although the SEM images exhibit a rich surface structure, the nanocomposite films were optically smooth. Film roughnesses were generally less than 10 nm as measured by atomic force microscopy.

XRD of the decomposed In_2Se_3 MCC precursor indicates the formation of γ-In_2Se_3 (Figure 1.4b), which is one of many In_2Se_3 polymorphs.[58] γ-In_2Se_3 has a defect wurtzite structure with 1/3 of the In sites vacant.[58, 59] Due to surface effects, it can be anticipated that the formation of thin film samples may exhibit morphological changes relative to powder samples. This effect is clearly observed when thermally decomposing In_2Se_3 MCC powder relative to spin-coated In_2Se_3 MCC thin films (Figures 1.4b-c). While the powder sample closely matches the γ-In_2Se_3 powder diffraction file, the thin film sample exhibits only a single diffraction peak corresponding to (0 0 6). This indicates that the grains in the γ-In_2Se_3 thin films preferentially orient themselves with the *ab*-plane parallel to the substrate. We are unaware of any literature reports on the surface energy of γ-In_2Se_3, but believe that these growth characteristics imply that the surface energy of γ-In_2Se_3 has significant crystallographic anisotropy. Since it is thermodynamically preferable for the γ-In_2Se_3 to minimize its free energy during growth, our observed growth characteristics imply that the low- and high-energy crystal facets of γ-In_2Se_3 are parallel and perpendicular to the *ab*-plane, respectively. By growing with the *ab*-plane parallel to the substrate, the surface area of the high-energy facets was minimized. It is worth noting that another common form of indium selenide, α-In_2Se_3, is also known to be highly anisotropic.[58, 60]

The strong crystallographic orientation preference of the In_2Se_3 is eliminated upon introducing CdSe nanocrystals into the composite, which indicates that the CdSe

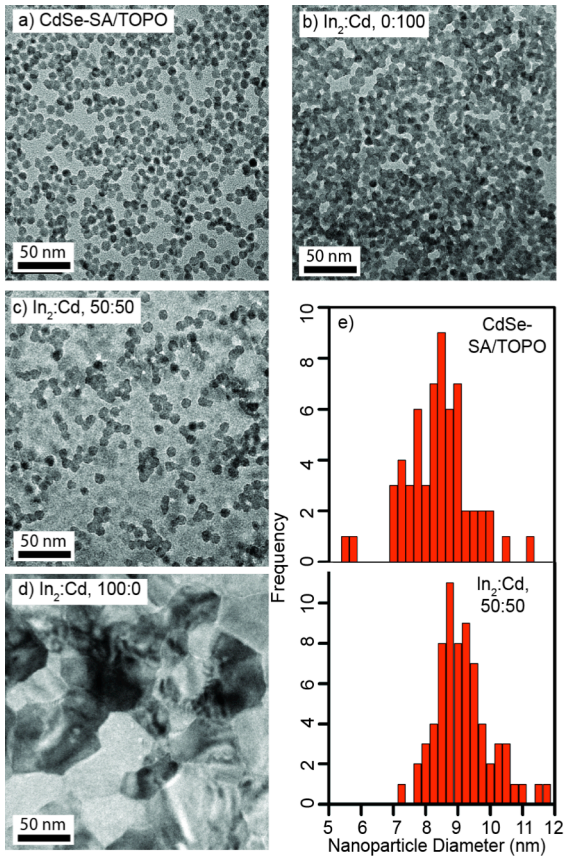

Figure 1.2. Transmission electron microscopy (TEM) images of (a) as-synthesized colloidal CdSe nanocrystals with a combination of stearic acid (SA) and trioctylphosphine oxide (TOPO) ligands and nanocomposites with In_2:Cd ratios of (b) 0:100, (c) 50:50, and (d) 100:0. Histograms illustrating the nanoparticle size distribution for the as-synthesized nanocrystals and the 50:50 composite are shown in part (e). The images in parts (b), (c), and (d) are of samples that have had their MCC precursor converted into In_2Se_3 by annealing at 350 °C for 30 minutes. The background contrast in images (a), (b), and (c) correspond to the carbon support film of the TEM grid, the Si_3N_4 TEM membrane, and γ-In_2Se_3 matrix, respectively.

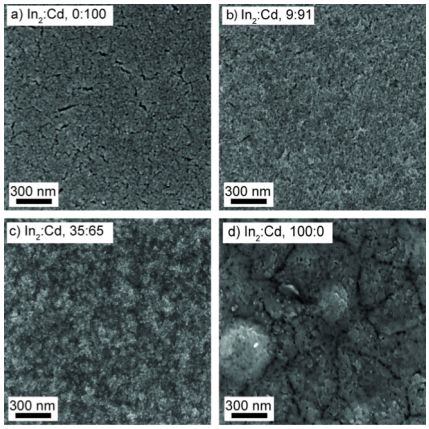

Figure 1.3. Scanning electron microscopy images of nanocomposites with In_2:Cd ratios of (a) 0:100, (b) 9:91, (c) 35:65, and (d) 100:0.

nanocrystals have a highly disruptive effect on the In_2Se_3 formation. This is indicated by the disappearance of the (0 0 6) In_2Se_3 reflection and appearance of new In_2Se_3 reflections. The large decrease in the signal:noise ratio of the XRD pattern upon inclusion of CdSe nanocrystals also indicates that the resulting In_2Se_3 grains are much smaller than in the 100% In_2Se_3 samples. This formation of smaller grains is corroborated by TEM images of the composites; In_2Se_3 grains are clearly resolved in the 100% In_2Se_3 images, but are not resolved upon introduction of CdSe nanocrystals (Figures 1.2c-d). This change in In_2Se_3 formation is likely due to the CdSe nanocrystals functioning as nucleation sites for In_2Se_3 crystallites. It is intuitive that the orientation of In_2Se_3 grains is random in the composites containing CdSe nanocrystals because the orientations of the CdSe nanocrystals themselves are randomized during deposition of the CdSe nanocrystal – MCC precursor mixture. It is also intuitive that the In_2Se_3 grain sizes are smaller in these composites because the presence of CdSe nanocrystals inhibits the formation of the large grains observed in the 100% In_2Se_3 samples.

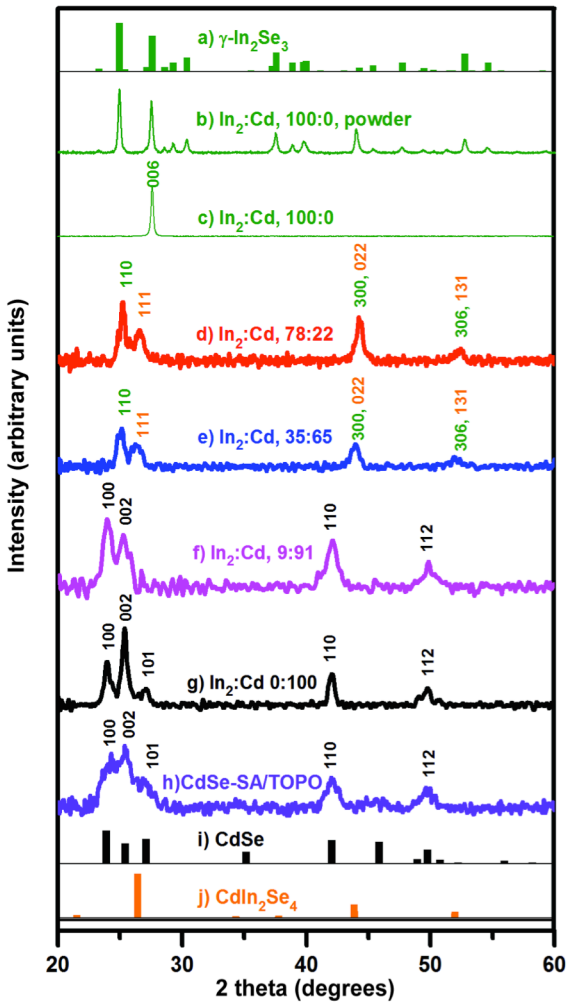

Figure 1.4. X-ray diffraction patterns of (a) γ-In_2Se_3 powder diffraction file 01-089-0658, (b) γ-In_2Se_3 powder, thin film nanocomposites with In_2:Cd ratios of (c) 100:0, (d) 78:22, (e) 35:65, and (f) 9:91, (g) 0:100 (h) as-synthesized colloidal CdSe nanocrystals with a combination of stearic acid (SA) and trioctylphosphine oxide (TOPO) ligands, (i) CdSe powder diffraction file 01-077-0021, and (j) $CdIn_2Se_4$ powder diffraction file 00-056-1124.

The observed CdSe diffraction peak widths in our composites demonstrate that the In_2Se_3 matrix inhibits CdSe nanocrystal merger and growth (Figure 1.4f-h). The broad peaks of the as-synthesized CdSe nanocrystals with organic ligands become notably sharper in the ~100% CdSe nanocomposite, which is indicative of an increase in CdSe crystallite size.[61] Scherrer analysis of the (1 1 0) peak in the as-synthesized CdSe colloidal nanocrystals and the ~100% CdSe composite yield grain sizes of 8 nm and 20 nm, respectively. This increase in crystallite size is also visible in the TEM images, which show a significant amount of nanocrystal fusing (Figure 1.2b). This crystallite growth is not surprising given the lack of matrix in between nanocrystals and the relatively high 350°C annealing temperatures used to make the composites. However, even a modest inclusion of In_2Se_3 into the composite, such as that of the 9:91 sample (Figure 1.4f), yields a noticeable decrease in CdSe diffraction peak sharpening. Scherrer analysis of the (1 1 0) peak in the 9:91 sample yields a grain size of 11 nm.

XRD characterization reveals the formation of a ternary phase, $CdIn_2Se_4$, in the nanocomposites and suggests a rich interaction between the CdSe nanocrystals and the In_2Se_3 matrix. Notably, only In_2Se_3 and $CdIn_2Se_4$ are observed in some of our XRD patterns (Figures 1.4d-e). While this qualitatively suggests the complete conversion of CdSe nanocrystals into $CdIn_2Se_4$ nanocrystals, such a conclusion would be oversimplified. For example, while our 35:65 sample shows only In_2Se_3 and $CdIn_2Se_4$ XRD peaks (Figure 1.4e), it is stoichiometrically

impossible for this sample to only form these compounds; stoichiometry would instead dictate the formation of CdSe and $CdIn_2Se_4$. This peculiarity can be explained by calculating the relative XRD peak intensities for CdSe and $CdIn_2Se_4$, which demonstrates that x-ray diffraction from $CdIn_2Se_4$ is inherently more intense than CdSe. The intensity of a XRD peak is proportional to $|S_{hkl}|^2 M_{hkl} / V_c^2$ where S_{hkl} and M_{hkl} are the structure factor and multiplicity factor of the *hkl* peak and V_c is the unit cell volume.[61] Values for the structure factor and multiplicity factor come from analysis of the crystallographic unit cell and symmetry, respectively. Calculation of these values show that the (1 1 1) peak of $CdIn_2Se_4$ is more intense than the (0 0 2) and (1 0 0) peaks of CdSe by factors of 3.7 and 6.8, respectively. Consequently it is not surprising that we can observe $CdIn_2Se_4$ diffraction without CdSe diffraction.

As mentioned in the earlier TEM discussion, the slight nanocrystal diameter growth from 8.2 nm to 9.0 nm in the 50:50 sample suggests the formation of a thin $CdIn_2Se_4$ layer at the interface between the CdSe nanocrystals and In_2Se_3 matrix. It is worth noting that the conversion of 8.2 nm CdSe nanocrystals into $CdIn_2Se_4$ via the addition of In and Se would result in 12.6 nm diameter nanocrystals, which are clearly not present in our TEM images. Nonetheless, it would still be possible to get 9.0 nm diameter $CdIn_2Se_4$ nanocrystals if Cd diffuses into the In_2Se_3 matrix. Consequently, while we believe a thin $CdIn_2Se_4$ layer between the CdSe nanocrystals and In_2Se_3 matrix is the most likely scenario, this cannot be definitively determined with the present data. Should the formation of ternary phases wish to be avoided, the use of other nanocrystal-matrix combinations with appropriate phase behavior could be used; for example, CdSe and $SnSe_2$ do not form ternary phases.[62] MCC precursors with low temperature decompositions such as that correspond to SnS_2,[63] Cu_2S,[64] or ZnTe[65] could also be used to limit elemental interdiffusion between the nanoparticles and matrix.

1.3.2. Nanocomposite Thermal Transport

Thermal transport in nanostructured materials is of interest for applications ranging from thermoelectricity, thermal barrier coatings, electronics thermal management, phase change memory, and heat assisted magnetic recording.[66] The structural motif of nanoparticles embedded in a crystalline matrix is a common theme in the thermal sciences community.[1-5, 7, 45, 46] It is well known that matrix-embedded nanoparticles promote broadband scattering of phonons, which correspondingly leads to low thermal conductivities. This is particularly important for thermoelectric applications wherein reduced thermal conductivities lead to large improvements in energy conversion efficiency.[1-5, 7] Notably CdSe alloyed with Hg has been investigated for its thermoelectrics properties.[67, 68] In addition, a stoichiometric variant of indium selenide, In_4Se_3, is one of the best bulk thermoelectric materials.[69] Inspired by these facts, we measured the thermal conductivity of our composites.

Figure 1.5 shows the room temperature thermal conductivity of the nanocomposites

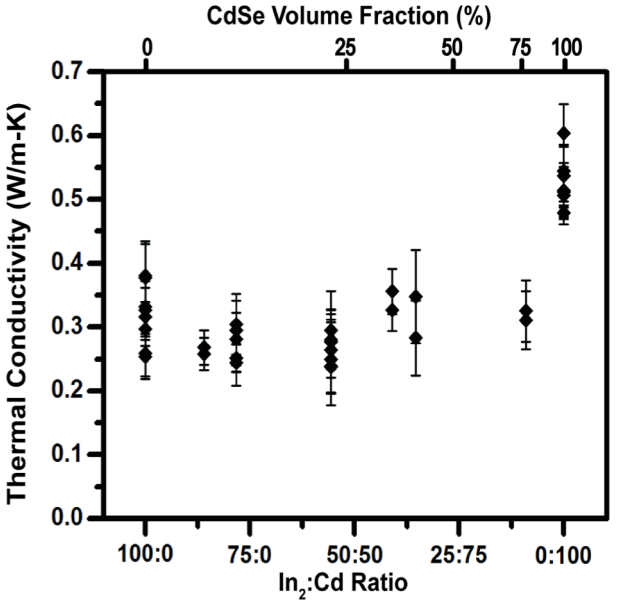

Figure 1.5. Thermal conductivity of nanocomposites with varying In_2:Cd ratios. Increasing amounts of Cd correspond to larger nanoparticle volume fractions in the composite. The upper horizontal axis indicates the nanocomposite's CdSe volume fraction in the limit of negligible $CdIn_2Se_4$ formation. Thermal conductivity measurements were done on multiple films and on up to two locations per film for each In_2:Cd ratio. All data points are shown above to best illustrate sample-to-sample and location-to-location variations.

as a function of In_2:Cd ratio. For reference purposes, the upper horizontal axis of Figure 1.5 indicates the CdSe volume fraction in the limit of negligible $CdIn_2Se_4$ formation. The 100% In_2Se_3 and ~100% CdSe samples have average thermal conductivities of 0.32 and 0.53 W/m-K, respectively. Surprisingly, the thermal conductivities of the mixed CdSe-In_2Se_3 composites were insensitive to the amount of CdSe and were ~ 0.3 W/m-K in all cases. These low thermal conductivities are comparable to amorphous polymers, which is quite remarkable for inorganic crystalline materials. No correlation between measured thermal conductivity and film thickness was observed. This indicates that thermal transport in these samples is diffusive and that the thermal contact resistances between layers of the 3ω thermal conductivity samples are negligible.

The thermal conductivity of our nanostructured γ-In_2Se_3 is a factor of 3 lower than other reports on polycrystalline γ-In_2Se_3.[53] Our lower thermal conductivity can be understood in the context of microstructural differences between our samples and those in the other report.[53] Yim *et al*.[53] prepared their samples via mechanical alloying and spark plasma sintering, which led to an isotropic polycrystalline sample with grain sizes spanning tens to hundreds of nanometers. In contrast, our samples are anisotropic and have relatively monodisperse grain sizes on the order of tens of nanometers. As seen in the TEM images, the lateral grain size of our samples (which, due to their preferential crystallographic orientation, corresponds to *ab*-plane) is 38 ± 12 nm (Figure 1.2d). Although we did not directly measure the cross-plane grain size, we infer that it is smaller than the lateral grain size as dictated by the Wulff construction.[70] The Wulff construction states that crystals grow slowest in directions perpendicular to their low energy surfaces, which in our case means that the smallest grain dimension should be in the cross-plane direction. The reduced grain sizes in our γ-In_2Se_3 relative to Yim *et al*.,[53] naturally leads to increased phonon scattering and reduced thermal conductivity.

Another factor leading to lower thermal conductivities in our γ-In_2Se_3 measurements is that we are probing transport along the *c*-axis. Since the low energy crystal facets in γ-In_2Se_3 are parallel to the *ab*-plane, the weakest bonds should be along the *c*-axis. This means that the phonon group velocities are slowest along the *c*-axis and as a consequence, the *c*-axis should be the crystallographic direction with lowest thermal conductivity. While it would be useful to assess the effect of this anisotropy by comparing to bulk single crystal γ-In_2Se_3 data, we note that thermal conductivity data in the literature is limited to polycrystalline In_2Se_3.[53, 71] We also note that although our measured thermal conductivity for γ-In_2Se_3 is quite low, it is still well above the minimum thermal conductivity predicted by the Cahill-Pohl model.[72] The Cahill-Pohl is often used to approximate the thermal conductivity of amorphous materials and is also commonly called the "minimum thermal conductivity model" and the "amorphous limit." The Cahill-Pohl model estimates a lower limit of 0.13 W/m-K for In_2Se_3; this is approximately a factor of 2.5 below our measured thermal conductivity and suggests even lower thermal conductivities for γ-In_2Se_3 are possible.

The thermal conductivity of our nanostructured CdSe is a factor of 17 lower than measurements on bulk single crystal CdSe.[51, 52] In fact, our average thermal conductivity of 0.53 W/m-K is near that of the Cahill-Pohl model, which predicts a lower limit of 0.40 W/m-K for CdSe.[72] A thermal conductivity this low suggests very intense phonon scattering in our ~100% CdSe composites. While thermal conductivity measurements on colloidal nanocrystals are relatively scarce, the existing literature shows that nanocrystal size and surface chemistry are the key factors determining thermal transport.[25, 44] Ong *et al.*[44] studied thermal transport in colloidal CdSe nanocrystals with varying surface chemistry and diameters ranging from 3.5 – 5.2 nm. Feser *et al.*[25] used colloidal nanocrystals to prepare polycrystalline CdSe with controlled grain sizes varying from 3.5 – 6.2 nm. The thermal conductivities in these prior works were on the order of 10^{-1} W/m-K, which is comparable to our results. However, extrapolating the results of Ong *et al.* and Feser *et al.* to the 20 nm grain size of our ~100% CdSe composites would yield thermal conductivity values greater than our measured value. The fact that our samples have larger grains,

but a comparable thermal conductivity, implies that phonon scattering at our interfaces is more intense (i.e. our grain boundaries have a lower phonon transmission probability).[73] This could be a result of the different CdSe crystallite surface chemistries in our work and these prior works. Feser *et al.* functionalized their CdSe nanocrystals with HgSe MCC precursor instead of the In_2Se_3 MCC precursor used in our work. Since CdSe and HgSe form a solid solution,[74] the grain boundary interfaces in the work by Feser *et al.* are very different than ours. While Ong *et al.* also studied CdSe nanocrystals with MCC precursor ligands, they did not thermally transform the MCC precursor into a metal-chalcogenide semiconductor and consequently their interfaces also differ from ours. Differences in phonon impurity scattering between our samples and these earlier works could also be affecting thermal transport. It should also be noted that mesoporosity differences in our samples and these prior works might also be leading to thermal transport dissimilarities.

With the exception of the ~100% CdSe sample, the thermal conductivities of our nanocomposites were surprisingly insensitive to CdSe volume fraction. The notable increase in thermal conductivity upon reaching ~100% CdSe likely arises from the increase in CdSe grain size that occurs in the absence of an In_2Se_3 matrix. We hypothesize the otherwise insensitive results to CdSe volume fraction arise from a variety of morphological changes that have competing effects on thermal conductivity. Since multiple morphological changes occur simultaneously in our composites, it is difficult to isolate the impact of any one change on thermal transport. Consequently we limit the discussion below to identifying these changes and qualitatively discussing their impact on thermal conductivity.

As CdSe is introduced into the In_2Se_3 matrix, the two most obvious morphological changes are a decrease in In_2Se_3 grain size and elimination of the preferential In_2Se_3 grain orientation. The decrease in In_2Se_3 grain size should reduce thermal conductivity due to increased phonon scattering at grain boundary interfaces. The elimination of the preferential In_2Se_3 grain orientation should increase thermal conductivity due to an increased phonon group velocity in the direction of thermal transport (i.e. as discussed earlier, the growth characteristics of the γ-In_2Se_3 imply that the phonon group velocity is slow along the *c*-axis and fast in the *ab*-plane).

Another important morphological change is the occurrence of CdSe-In_2Se_3 grain boundaries. In the simple case of isotropic crystal structures, one would expect this to reduce thermal conductivity. This is because compositionally-mismatched grain boundaries should have a greater acoustic impedance mismatch than compositionally-matched grain boundaries, which consequently leads to larger thermal interface resistances.[73] However, in our case the net effect of CdSe-In_2Se_3 grain boundaries is ambiguous due to the anisotropy of the In_2Se_3 grains. Crystalline anisotropy causes thermal interface resistance to be a function of both composition and grain orientation. This dependency has been both previously modeled[75] and experimentally demonstrated.[76] Although we could not find literature for the speed of sound anisotropy in γ-In_2Se_3, we note that the speed of sound anisotropy in α-In_2Se_3 is significant, ~70% for the longitudinal phonon mode.[60] We also note that the acoustic impedance mismatch in our grain boundaries is dominated by the speed of sound since the densities of CdSe and In_2Se_3 only differ by ~6%. Due to these grain orientation effects, some fraction of the In_2Se_3-In_2Se_3 grain boundaries likely have larger thermal interface resistances than CdSe-In_2Se_3 grain boundaries and vice versa. Consequently the relative impact of In_2Se_3-In_2Se_3 versus In_2Se_3-CdSe grain boundaries on thermal conductivity is ambiguous.

Yet another important morphological change is the formation of $CdIn_2Se_4$. As mentioned earlier, this $CdIn_2Se_4$ likely forms at the interface between the CdSe nanocrystals and the In_2Se_3 matrix, and so would also affect the CdSe-In_2Se_3 thermal interface resistance. If the $CdIn_2Se_4$ layer is very thin, it can have an interface "smoothing" effect[77] that decreases thermal interface resistance and thereby increases nanocomposite thermal conductivity. On the other hand, if the $CdIn_2Se_4$ is thick enough, two distinct interfaces could arise, CdSe-$CdIn_2Se_4$ and $CdIn_2Se_4$-In_2Se_3.

The combined thermal resistance of these two interfaces could be larger than that of a single CdSe-In_2Se_3 interface and thereby decrease nanocomposite thermal conductivity.

Regardless of its precise origins, this thermal conductivity insensitivity to CdSe volume fraction suggests that low thermal conductivities can be reliably achieved using this solution-phase synthesis route to nanocomposite materials. Since these thermal conductivities are already attractively low for thermoelectrics, future work measuring the other thermoelectric properties (i.e. electrical conductivity and Seebeck coefficient) is merited. Furthermore, studies using the recently-developed colloidal nanocrystal chemistries that yield charge mobilities near single-crystal values would be especially promising.[35]

1.4. Conclusions

The synthesis and characterization of nanocomposites with variable nanoparticle volume fraction made by combining CdSe nanocrystals and In_2Se_3 MCC precursor has been presented. We observe rich structural and chemical interactions between the CdSe nanocrystals and the In_2Se_3 matrix during composite formation. These interactions include alterations in In_2Se_3 grain size and orientation as well as the formation of a ternary phase, $CdIn_2Se_4$. The thermal conductivity of these composites is on the order of 10^{-1} W/m-K over the entire nanoparticle volume fraction range, which is remarkably low for inorganic crystalline materials and is comparable to amorphous polymers. With the exception of the ~100% CdSe samples, the thermal conductivity of the nanocomposite is insensitive to CdSe volume fraction. We attribute this insensitivity to competing effects that arise from structural morphology changes as the composite is formed.

1.5. Section 1 References

1 Biswas, K.; He, J.; Blum, I. D.; Wu, C. I.; Hogan, T. P.; Seidman, D. N.; Dravid, V. P.; Kanatzidis, M. G. *Nature* 2012**, 489**, 414-418.

2 Dresselhaus, M. S.; Chen, G.; Tang, M. Y.; Yang, R. G.; Lee, H.; Wang, D. Z.; Ren, Z. F.; Fleurial, J. P.; Gogna, P. *Adv. Mater.* 2007**, 19**, 1043-1053.

3 Liu, W.; Yan, X.; Chen, G.; Ren, Z. *Nano Energy* 2012**, 1**, 42-56.

4 Mingo, N.; Hauser, D.; Kobayashi, N. P.; Plissonnier, M.; Shakouri, A. *Nano Lett.* 2009**, 9**, 711-715.

5 Kim, W.; Zide, J.; Gossard, A.; Klenov, D.; Stemmer, S.; Shakouri, A.; Majumdar, A. *Phys. Rev. Lett.* 2006**, 96**, 045901.

6 Wang, R. Y.; Feser, J. P.; Lee, J. S.; Talapin, D. V.; Segalman, R.; Majumdar, A. *Nano Lett.* 2008**, 8**, 2283-2288.

7 Biswas, K.; He, J. Q.; Zhang, Q. C.; Wang, G. Y.; Uher, C.; Dravid, V. P.; Kanatzidis, M. G. *Nat. Chem.* 2011**, 3**, 160-166.

8 Liu, M.; Ma, Y.; Wu, H.; Wang, R. Y. *ACS Nano* 2015**, 9**, 1341-1351.

9 Liu, M. L.; Wang, R. Y. *Nanoscale* 2013**, 5**, 7234-7237.

10 Talapin, D. V.; Lee, J. S.; Kovalenko, M. V.; Shevchenko, E. V. *Chem. Rev.* 2010**, 110**, 389-458.

11 Chuang, C. H. M.; Brown, P. R.; Bulovic, V.; Bawendi, M. G. *Nat. Mater.* 2014**, 13**, 796-801.

12 Caldwell, M. A.; Jeyasingh, R. G. D.; Wong, H. S. P.; Milliron, D. J. *Nanoscale* 2012**, 4**, 4382-4392.

13 Sun, S. H.; Murray, C. B.; Weller, D.; Folks, L.; Moser, A. *Science* 2000**, 287**, 1989-1992.

14 Llordes, A.; Garcia, G.; Gazquez, J.; Milliron, D. J. *Nature* 2013**, 500**, 323-326.

15 Runnerstrom, E. L.; Llordes, A.; Lounis, S. D.; Milliron, D. J. *Chem. Commun.* 2014**, 50**, 10555-10572.

16 Dabbousi, B. O.; Bawendi, M. G.; Onitsuka, O.; Rubner, M. F. *Appl. Phys. Lett.* 1995**, 66**, 1316-1318.

17 Trindade, T.; Neves, M. C.; Barros, A. M. V. *Scr. Mater.* 2000**, 43**, 567-571.

18 Guglielmi, M.; Martucci, A.; Menegazzo, E.; Righini, G. C.; Pelli, S.; Fick, J.; Vitrant, G. *J. Sol-Gel Sci. Technol.* 1997**, 8**, 1017-1021.
19 Mokari, T.; Sertchook, H.; Aharoni, A.; Ebenstein, Y.; Avnir, D.; Banin, U. *Chem. Mater.* 2005**, 17**, 258-263.
20 Llordes, A.; Hammack, A. T.; Buonsanti, R.; Tangirala, R.; Aloni, S.; Helms, B. A.; Milliron, D. J. *J. Mater. Chem.* 2011**, 21**, 11631-11638.
21 Kovalenko, M. V.; Scheele, M.; Talapin, D. V. *Science* 2009**, 324**, 1417-1420.
22 Tangirala, R.; Baker, J. L.; Alivisatos, A. P.; Milliron, D. J. *Angew. Chem., Int. Ed.* 2010**, 49**, 2878-2882.
23 Mitzi, D. B.; Copel, M.; Chey, S. J. *Adv. Mater.* 2005**, 17**, 1285-1289.
24 Milliron, D. J.; Raoux, S.; Shelby, R.; Jordan-Sweet, J. *Nat. Mater.* 2007**, 6**, 352-356.
25 Feser, J. P.; Chan, E. M.; Majumdar, A.; Segalman, R. A.; Urban, J. J. *Nano Lett.* 2013**, 13**, 2122-2127.
26 Mitzi, D. B. *Adv. Mater.* 2009**, 21**, 3141-3158.
27 Nag, A.; Zhang, H.; Janke, E.; Talapin, D. V. *Z. Phys. Chem. (Muenchen, Ger.)* 2015**, 229**, 85-107.
28 Nag, A.; Kovalenko, M. V.; Lee, J. S.; Liu, W.; Spokoyny, B.; Talapin, D. V. *J. Am. Chem. Soc.* 2011**, 133**, 10612-10620.
29 Zhang, H.; Jang, J.; Liu, W.; Talapin, D. V. *ACS Nano* 2014**, 8**, 7359-7369.
30 Liu, W.; Lee, J. S.; Talapin, D. V. *J. Am. Chem. Soc.* 2013**, 135**, 1349-1357.
31 Ko, D. K.; Kang, Y.; Murray, C. B. *Nano letters* 2011**, 11**, 2841-2844.
32 Choi, J. H.; Fafarman, A. T.; Oh, S. J.; Ko, D. K.; Kim, D. K.; Diroll, B. T.; Muramoto, S.; Gillen, J. G.; Murray, C. B.; Kagan, C. R. *Nano Lett.* 2012**, 12**, 2631-2638.
33 Chung, D. S.; Lee, J. S.; Huang, J.; Nag, A.; Ithurria, S.; Talapin, D. V. *Nano Lett.* 2012**, 12**, 1813-1820.
34 Lee, J. S.; Kovalenko, M. V.; Huang, J.; Chung, D. S.; Talapin, D. V. *Nature nanotechnology* 2011**, 6**, 348-352.
35 Dolzhnikov, D. S.; Zhang, H.; Jang, J.; Son, J. S.; Panthani, M. G.; Shibata, T.; Chattopadhyay, S.; Talapin, D. V. *Science* 2015**, 347**, 425-428.
36 Kim, D. K.; Lai, Y.; Diroll, B. T.; Murray, C. B.; Kagan, C. R. *Nat Commun* 2012**, 3**, 1216.
37 Yun, H. J.; Paik, T.; Edley, M. E.; Baxter, J. B.; Murray, C. B. *ACS Appl. Mater. Interfaces* 2014**, 6**, 3721-3728.
38 Yang, D.; Lu, C.; Yin, H.; Herman, I. P. *Nanoscale* 2013**, 5**, 7290-7296.
39 Zhang, Y.; Snedaker, M. L.; Birkel, C. S.; Mubeen, S.; Ji, X.; Shi, Y.; Liu, D.; Liu, X.; Moskovits, M.; Stucky, G. D. *Nano letters* 2012**, 12**, 1075-1080.
40 Han, M.-K.; Kim, S.; Kim, H.-Y.; Kim, S.-J. *RSC Advances* 2013**, 3**, 4673.
41 Cadavid, D.; Ibáñez, M.; Shavel, A.; Durá, O. J.; López de la Torre, M. A.; Cabot, A. *Journal of Materials Chemistry A* 2013**, 1**, 4864.
42 Kovalenko, M. V.; Spokoyny, B.; Lee, J. S.; Scheele, M.; Weber, A.; Perera, S.; Landry, D.; Talapin, D. V. *J. Am. Chem. Soc.* 2010**, 132**, 6686-6695.
43 Wang, R. Y.; Tangirala, R.; Raoux, S.; Jordan-Sweet, J. L.; Milliron, D. J. *Adv. Mater.* 2012**, 24**, 99-103.
44 Ong, W. L.; Rupich, S. M.; Talapin, D. V.; McGaughey, A. J.; Malen, J. A. *Nat. Mater.* 2013**, 12**, 410-415.
45 Pernot, G.; Stoffel, M.; Savic, I.; Pezzoli, F.; Chen, P.; Savelli, G.; Jacquot, A.; Schumann, J.; Denker, U.; Monch, I.; Deneke, C.; Schmidt, O. G.; Rampnoux, J. M.; Wang, S.; Plissonnier, M.; Rastelli, A.; Dilhaire, S.; Mingo, N. *Nat. Mater.* 2010**, 9**, 491-495.
46 Kim, W. W., R.Y. ; Majumdar,A. *Nano Today* 2007**, 2**, 40-47.
47 Poudel, B.; Hao, Q.; Ma, Y.; Lan, Y.; Minnich, A.; Yu, B.; Yan, X.; Wang, D.; Muto, A.; Vashaee, D.; Chen, X.; Liu, J.; Dresselhaus, M. S.; Chen, G.; Ren, Z. *Science* 2008**, 320**, 634-638.

48 Lee, H.; Lan, Y.; Wang, X. W.; Zhu, G.; Dresselhaus, M. S.; Chen, G.; Ren, Z. *Nano Lett.* 2008**,** **8**, 4670-4674.
49 Zhang, H.; Minnich, A. J. *Scientific reports* 2015**,** **5**, 8995.
50 LeBlanc, S.; Yee, S. K.; Scullin, M. L.; Dames, C.; Goodson, K. E. *Renewable and Sustainable Energy Reviews* 2014**,** **32**, 313-327.
51 Ioffe, A. V.; Ioffe, A. F. *Soviet Physics-Solid State* 1960**,** **2**, 719-728.
52 Slack, G. A. *Phys. Rev. B* 1972**,** **6**, 3791-3800.
53 Yim, J.-H.; Park, H.-H.; Jang, H. W.; Yoo, M.-J.; Paik, D.-S.; Baek, S.; Kim, J.-S. *J. Electron. Mater.* 2012**,** **41**, 1354-1359.
54 Qu, L. H. P., Z.A; Peng,X.G;. *Nano Lett.* 2001**,** **1**, 333-337.
55 Borca-Tasciuc, T.; Kumar, A. R.; Chen, G. *Rev. Sci. Instrum.* 2001**,** **72**, 2139-2147.
56 Cahill, D. G. *Rev. Sci. Instrum.* 1990**,** **61**, 802-808.
57 Lee, S. M.; Cahill, D. G. *J. Appl. Phys.* 1997**,** **81**, 2590-2595.
58 Han, G.; Chen, Z. G.; Drennan, J.; Zou, J. *Small* 2014**,** **10**, 2747-2765.
59 Ye, J. P.; Soeda, S.; Nakamura, Y.; Nittono, O. *Jpn. J. Appl. Phys., Part 1* 1998**,** **37**, 4264-4271.
60 Raranskii, N. D.; Balazyuk, V. N.; Kovalyuk, Z. D.; Mel'nik, N. I.; Gevik, V. B. *Inorg. Mater.* 2011**,** **47**, 1174-1177.
61 Howe, J.; Fultz, B., *Transmission Electron Microscopy and Diffractometry of Materials*. 3rd ed.; Springer: New York, 2008.
62 Galiulin, E. A.; Odin, I. N.; Novoselova, A. V. *Zh. Neorg. Khim.* 1982**,** **27**, 266-268.
63 Mitzi, D. B.; Kosbar, L. L.; Murray, C. E.; Copel, M.; Afzali, A. *Nature* 2004**,** **428**, 299-303.
64 Mitzi, D. B. *Inorg. Chem.* 2007**,** **46**, 926-931.
65 Mitzi, D. B. *Inorg. Chem.* 2005**,** **44**, 7078-7086.
66 Cahill, D. G.; Braun, P. V.; Chen, G.; Clarke, D. R.; Fan, S. H.; Goodson, K. E.; Keblinski, P.; King, W. P.; Mahan, G. D.; Majumdar, A.; Maris, H. J.; Phillpot, S. R.; Pop, E.; Shi, L. *Appl. Phys. Rev.* 2014**,** **1**, 011305.
67 Cruceanu, E.; Ionescub.S. *J. Mater. Sci.* 1969**,** **4**, 570-573.
68 Sofo, J. O. *J. Appl. Phys.* 1995**,** **77**, 1561-1563.
69 Rhyee, J. S.; Lee, K. H.; Lee, S. M.; Cho, E.; Il Kim, S.; Lee, E.; Kwon, Y. S.; Shim, J. H.; Kotliar, G. *Nature* 2009**,** **459**, 965-968.
70 Wulff, G. *Zeitschrift Fur Krystallographie Und Mineralogie* 1901**,** **34**, 449-530.
71 Sirota, N. N.; Berger, L. I. *Inzh.-Fiz. Zh.* 1958**,** **1**, 117-120.
72 Cahill, D. G.; Watson, S. K.; Pohl, R. O. *Phys. Rev. B* 1992**,** **46**, 6131-6140.
73 Swartz, E. T.; Pohl, R. O. *Rev. Mod. Phys.* 1989**,** **61**, 605-668.
74 Gavaleshko, N. P.; Gorlei, P. N.; Paranchich, S. Y.; Frasunyak, V. M.; Khomyak, V. V. *Inorg. Mater.* 1983**,** **19**, 298-300.
75 Duda, J. C.; Smoyer, J. L.; Norris, P. M.; Hopkins, P. E. *Appl. Phys. Lett.* 2009**,** **95**, 031912.
76 Hopkins, P. E.; Beechem, T.; Duda, J. C.; Hattar, K.; Ihlefeld, J. F.; Rodriguez, M. A.; Piekos, E. S. *Phys. Rev. B* 2011**,** **84**.
77 English, T. S.; Duda, J. C.; Smoyer, J. L.; Jordan, D. A.; Norris, P. M.; Zhigilei, L. V. *Phys. Rev. B* 2012**,** **85**, 035438.

2.0 Modifying Thermal Transport in Colloidal Nanocrystal Solids with Surface Chemistry

2.1. Introduction

Colloidal nanocrystals (NCs) are an important class of nanoparticle that can be synthesized with precise size, shape, and composition. This morphological control enables excellent control over NC properties and facilitates their use as building blocks for nanocomposites with novel and tunable properties that are unachievable in bulk materials.[1-3] One commonly studied NC-based material is the colloidal NC solid, which consists of a densely packed array of colloidal NCs. These colloidal NC solids have been employed across a wide range of applications including light emitting diodes (LEDs),[4, 5] photovoltaics,[6, 7] electronics,[8, 9] thermal storage,[3, 10] and thermoelectrics.[11, 12] In each of these applications, thermal transport properties play an important role. For example, a high thermal conductivity is desirable for LEDs, photovoltaics, and electronics because this minimizes temperature rise during operation, which improves both device performance and lifetime. A high thermal conductivity is also beneficial for thermal storage because it facilitates fast thermal charging/discharging. In contrast, a low thermal conductivity is ideal for thermoelectric applications because this improves efficiency in thermoelectric coolers and generators. Despite the importance of thermal conductivity in each of these applications, experimental data on thermal transport in NC solids is very limited.[13]

Colloidal NCs consist of an inorganic crystalline core with ligands bound to its surface. The native ligands on colloidal NCs are typically bulky organic molecules (*e.g.* oleic acid, trioctylphosphine oxide, alkanethiols, *etc*.). These native ligands help control the nucleation and growth of colloidal NCs during synthesis and are hence necessary from a synthetic perspective. However, these native ligands are generally undesirable from a functional materials perspective (*e.g.* electrically insulating). Previous studies have shown that the choice of ligands dramatically affects NC properties,[14-20] and it is now a common practice to replace the native ligands with new ligands that impart desirable properties. For example, by replacing the native dodecanethiol ligands with metal chalcogenide complexes, the electrical conductivity of Au NC solids was increased by 10 orders of magnitudes.[18] In another example, the optical absorption of PbS NCs was increased by a factor of 3 through the use of short conjugated ligands.[19] In addition to these intended effects on electrical and optical properties, it is important to understand how ligand choice affects thermal transport.

Thermal transport in NC solids was first experimentally studied by Ong *et al*.[13] They found very low thermal conductivities and that NC diameter had the biggest impact on this property. They also conducted limited experiments on ligand-exchanged NC solids and found moderate thermal conductivity increases of ~ 50%. A couple of molecular dynamics studies have since confirmed the importance of NC diameter on thermal transport and also identified the NC core-ligand interface as an important parameter.[21, 22] While these studies are important landmarks in the study of thermal transport in NC solids, important questions regarding the effect of surface chemistry remain. How does the ligand's binding group and backbone length affect thermal transport in NC solids? Can ligand exchange increase NC solid thermal conductivity beyond the moderate 50% demonstrated by Ong *et al.*? How is the impact of surface chemistry on thermal transport affected by NC diameter?

To address these questions, we study thermal transport in PbS NC solids and systematically vary NC diameter and ligand structure. Our choice of PbS as a model system is motivated by the technological importance of PbS NC solids to optoelectronic applications, such as photodetectors[6, 23] and photovoltaics.[7, 16, 24] In addition, PbS is among the most well understood colloidal NCs and there is a wide body of literature detailing its structure,[25, 26] properties,[27, 28] and behavior.[29, 30] The native ligands on the PbS NCs in this study are oleic acid (OA) and we exchange these with ligands of varying backbone length (ethanedithiol, butanedithiol, hexanedithiol and octanedithiol) and different binding groups (thiols, amines, and halides). Our experiments reveals several findings: (i) The choice of ligand can increase the thermal conductivity of NC solids by up to ~ 150%. (ii) The ligand binding strength to the NC core does not significantly impact thermal conductivity. (iii) Reducing the ligand length can decrease the

interparticle distance, which increases thermal conductivity. (iv) Increasing the NC diameter increases thermal conductivity. (v) The effect of surface chemistry can exceed the effect of NC diameter and becomes more pronounced as NC diameter decreases. By combining these trends, we demonstrate that the thermal conductivity of NC solids can be varied by an overall factor of 4, from ~ 0.1-0.4 W/m-K. We complement these thermal transport findings with effective medium approximation (EMA) modeling and identify thermal transport in the ligand matrix as the rate-limiting factor for heat transfer. By combining our experimental observations with these modeling results, we conclude that future efforts to increase thermal conductivity in NC solids should focus on the ligand-ligand interactions between neighboring NCs.

2.2. Materials and Methods

2.2.1. Materials and Equipment

Lead oxide (99.999%), bis(trimethylsilyl)sulfide (TMS, synthesis grade), oleic acid (OA, 90%), 1-octadecene (ODE, 90%), tetrabutylammonium iodide (TBAI, 98%+), cetrimonium bromide (CTAB, 99%), 1,2- ethanedithiol (EDT, 98%+), 1,4-butanedithiol (BDT, 97%+), 1,6-hexanedithiol (HDT, 96%+), 1,8-octanedithiol (ODT, 97%+), ethylenediamine (EDA, 99%), methanol (anhydrous 99.8%), acetonitrile (anhydrous 99.8%), octane (98%), were purchased from Sigma Aldrich and used as received. Sample imaging was done with transmission electron microscopy (TEM, Tecnai F20) and scanning electron microscopy (SEM, Nova 200 NanoLab FEI). The X-ray diffraction was taken on high resolution PANalytical x-ray diffractometer, with CuKα X-ray source operating at 40 kV and 40 mA. The x-ray reflectivity measurements were also done using the PANalytical x-ray diffractometer. Fourier transform infrared spectroscopy measurements were done using a Thermo Nicolet 6700 system equipped with Smart SAGA accessory. Thickness measurements were carried out using atomic force microscopy (Digital Instrument Dimension 3000) and profilometry (Dektek II surface profilometer). For thermal conductivity measurements, a Keithley 6221 was used as the current source and a Stanford Research Systems SR830 lock-in amplifier was used to measure the 1st and 3rd harmonic voltage signals.

2.2.2. Nanocrystal Synthesis

PbS colloidal NCs were synthesized by employing the hot injection technique reported by Hines *et al.*[31] with minor modifications. In a typical synthesis of 3 nm PbS NCs, 0.45 g of lead oxide was dissolved in a solvent mixture of 2 mL OA and 18 mL ODE, and degassed by heating under vacuum at 100 °C for 2 hours. After all of the solid dissolved and the solution turned transparent, the temperature was increased to 145 °C, at which point a mixture of 10 mL ODE and 210 µL TMS was injected. The heating mantle was removed from the reaction flask right after the TMS injection, and then replaced when the temperature dropped to 100 °C. The reaction mixture was slowly cooled to ~ 30 °C with the heating mantle in place and turned off. PbS NCs were then separated from the reaction mixture by precipitating with ethanol and resuspending with hexane. This precipitation/suspension process was carried out 3 times in total. To vary NC diameter, the ratio of OA:ODE was varied; higher OA concentration led to larger diameters. The diameters of the PbS NCs used in this study were 3.3 ± 0.3 nm, 4.2 ± 0.4 nm, 5.8 ± 0.4 nm and 8.2 ± 0.7 nm.

2.2.3.Layer-by-Layer (LBL) Ligand Exchange

Ligand exchange in all NC solid films were done using a solid-state ligand exchange process in a LBL fashion. Prior to film deposition, all NCs were precipitated and resuspended an additional 3 times. The NCs were suspended in octane with a concentration of 10 - 15 mg/mL for the film deposition. For each layer deposition, ~ 70 µL PbS NC suspension was dispensed onto a 20 mm x 20 mm silicon substrate and spin coated at a speed of 3000 rpm for 1 min. Then, ~ 200 µL of the ligand solution was dispensed onto the NC solid thin film, allowed to rest for 30 s, and then removed by spin drying. The NC solid film was then flooded by ~ 200 µL of pure solvent and then spun dry to remove unbound ligands. The NC solid was then flooded with solvent and spun dry an additional 2 times. Depending on NC size and ligand, each layer deposition resulted in a thin film between 10 - 25 nm. Typically, 6 - 10 layers of NC solid were

deposited to yield an appropriate film thickness for thermal conductivity measurements (~ 100 - 180 nm). Thinner films made *via* 2-3 layer deposition cycles (~ 20 – 30 nm) were used for measuring mass density *via* x-ray reflectivity. The ligand solutions were prepared as suggested by previous studies:[30, 33] CTAB and TBAI, 30 mM in methanol; EDA, 1 M in methanol; EDT, 1.7 mM in acetonitrile; BDT, 2.5 mM in acetonitrile; HDT, 4 mM in acetonitrile; and ODT, 8 mM in acetonitrile.

2.2.4. Film Thickness Measurement

Thickness measurements on all ligand exchanged NC solid samples were determined by profilometry measurements. NC films were scratched using tweezers and the film thickness measured at the scratch location. The film thickness was determined by averaging measured thicknesses from 3 scans at different locations. The typical thickness variation of a film was found within 10 nm. NC solids with OA ligands were too soft to have their thickness measured with profilometry and were instead measured with atomic force microscopy.

2.2.5. Thermal Conductivity Measurement

Thermal conductivity measurements were performed using the differential 3ω method,[45] which is a widely used technique for thin film geometries.[46, 47] To prepare samples for measurement, NC solid films were first coated with a ~ 150 nm Al_2O_3 dielectric layer. Al metal lines, which function as combined heaters and thermometers, were then deposited on the samples using a shadow mask. The line dimensions in all samples were 45 μm wide, 2.6 mm long, and 150 nm thick. An AC current was run through the Al line to operate it as a heat source and the third harmonic of the voltage response was measured to operate the Al line as a thermometer. In accordance with the differential technique, a reference sample with only dielectric layer and silicon substrate was identically prepared. The thermal response of the NC solid thin film was obtained by subtracting the thermal response of the reference sample from the experimental sample. To convert 3ω electrical signals into thermal responses, the temperature coefficient of resistance (TCR) of 3ω lines were measured using a home-built thermal stage. In this measurement, the resistances of the 3ω lines were measured at 5 different temperature points between 15°C and 30°C, and a linear fit was used to determine the slope.

2.3. Results and discussion

We synthesized PbS NCs with OA ligands using the hot-injection method described by Hines *et al*.[31] Figure 2.1b shows a representative transmission electron microscopy image of the PbS NCs made using this approach and x-ray diffraction confirms the crystalline structure of the PbS core (Figure 2.1d). Varying the reaction conditions enabled NC diameter control from 3.3 to 8.2 nm. After synthesis, the PbS NCs were spin-coated onto silicon substrates to yield a NC solid thin film (Figures 2.1a and 2.1c). The native OA ligands were then replaced with new ligands using a solid-state process. Seven different surface treatments were performed in this study: 1,2-ethanedithiol (EDT), 1,4-butanedithiol (BDT), 1,6-hexanedithiol (HDT), 1,8-octanedithiol (ODT), ethylenediamine (EDA), tetrabutylammonium iodide (TBAI), and cetrimonium bromide (CTAB). The structures of these molecules are illustrated in Figure 2.2b. We note that treating PbS NCs with TBAI and CTAB results in an NC surface that is terminated with I^- and Br^-, respectively (*i.e.* the bulky organic component of these molecules washes away during the ligand exchange process).[7, 16, 32] For simplicity purposes, we refer to these as I^- and Br^- ligands throughout this paper. Fourier transform infrared spectroscopy

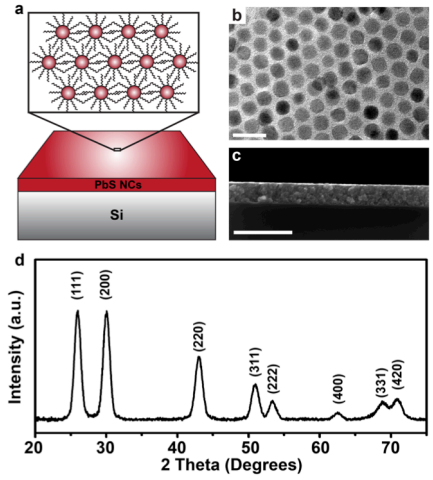

Figure 2.1. (a) Schematic of a PbS nanocrystal solid thin film on a silicon substrate. (b) A transmission electron microscopy image of 8.2 ± 0.7 nm PbS nanocrystals with native oleic acid ligands (the scale bar is 20 nm). (c) Cross-sectional scanning electron microscopy image showing a nanocrystal solid thin film that consists of 8.2 nm PbS nanocrystals with I^- ligands (the scale bar is 500 nm). (d) X-ray diffraction pattern of an 8.2 nm PbS nanocrystal solid thin film with oleic acid ligands.

measurements confirm the success of these ligand exchanges (Figure 2.2a). The absence of the native OA ligands is indicated by the lack of COO^- and C = C absorptions, which are at 1500-1700 cm^{-1}, in all ligand exchanged samples.

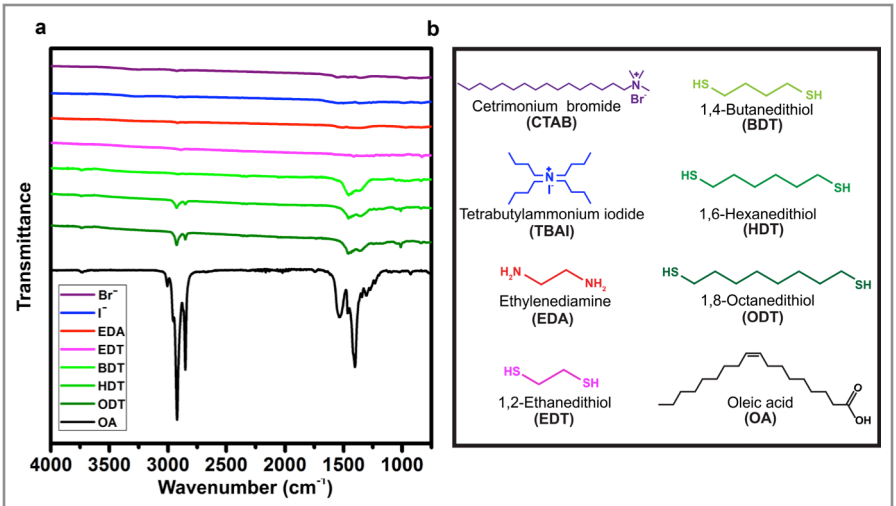

Figure 2.2. (a) Fourier transform infrared spectra of PbS nanocrystal solids with various ligands. (b) The chemical structure of the molecules used during ligand exchange. Note that treating PbS nanocrystals with tetrabutylammonium iodide (TBAI) and cetrimonium bromide (CTAB) results in nanocrystal surface terminations of I^- and Br^-, respectively [References 16 and 32].

To prepare high-quality film for thermal conductivity measurements, we carried out the solid-state ligand exchange process using a layer-by-layer (LBL) approach (Figure 2.3a).[30, 33, 34] Each layer was prepared in three steps: a) Depositing a thin layer of PbS NCs with OA ligands *via* spin coating; b) Immersing the NC solid film in a solution containing the desired ligand (typically 30 s) and spinning dry; c) Removing unbound ligand molecules by repeatedly flooding the NC solid film with pure solvent and spinning dry. Depending on the NC diameter and ligand choice, each layer deposition resulted in a NC solid thin film of 10-25 nm. This deposition process was then repeated 6-10 times to yield thicker films (100-180 nm) that are appropriate for thermal conductivity measurements. Films prepared by this approach exhibited excellent film quality with minimal porosity/cracking (Figure 2.3b). In contrast, NC solid films prepared *via* one-time solid-state ligand exchange on thick films exhibited extensive/deep cracking that made them unsuitable for transport measurements.

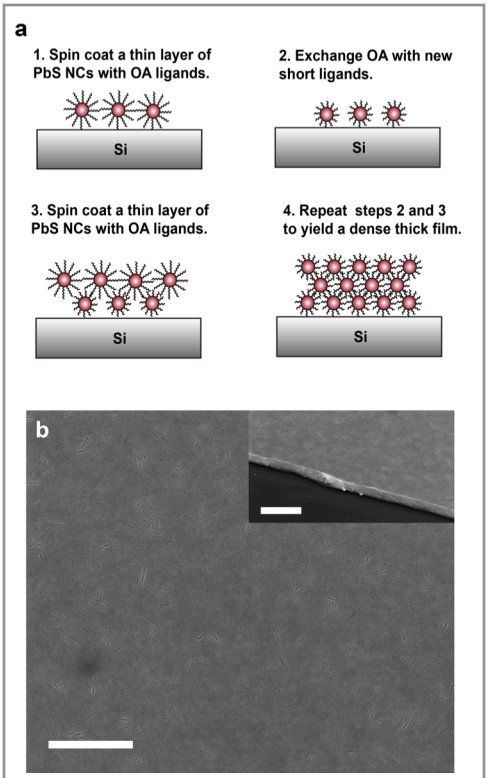

Figure 2.3. (a) Schematic illustrating the solid-state, layer-by-layer ligand exchange technique used to prepare nanocrystal (NC) solid films. This layer-by-layer technique minimizes film cracking during exchange of the long oleic acid (OA) ligands with new short ligands. (b) Scanning electron microscopy image of a 3.3 nm PbS NC solid with ethanedithiol ligands. The inset in part (b) shows an angled view of the NC solid film that confirms dense NC packing throughout the film thickness. The scale bar in both images is 1 μm.

We first investigate the effect of the ligand's binding group on the NC solid thermal conductivity (Figure 2.4). This is motivated by past thermal transport studies on a closely related cousin to colloidal NCs, self-assembled monolayer (SAM) junctions.[35, 36] SAMs are molecular monolayers adsorbed onto planar solid surfaces[37] and prior work has shown an increasing thermal interface conductance as the binding strength between the SAM molecules and solid surface increases.[35, 36] In effect, we ask ourselves whether this correlation between binding strength and thermal transport can be realized in the more complex structure of NC solids. To investigate this, we compare the thermal conductivity of 3.3 nm diameter PbS NC solids with EDA and EDT ligands. These two ligands have identical backbones, but different binding groups: amine groups for EDA and thiol groups for EDT. Both of these groups form covalent bonds to PbS NCs, although it is known that the thiol group forms a stronger bond.[38] Interestingly, we

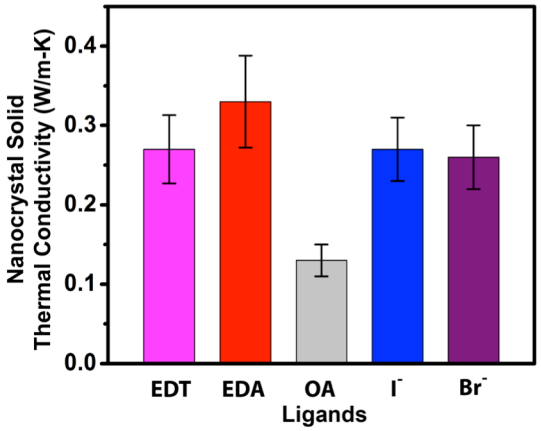

Figure 2.4. Thermal conductivity of 3.3 nm PbS nanocrystal solids with ethanedithiol (EDT), ethylenediamine (EDA), oleic acid (OA), I^-, and Br^- ligands.

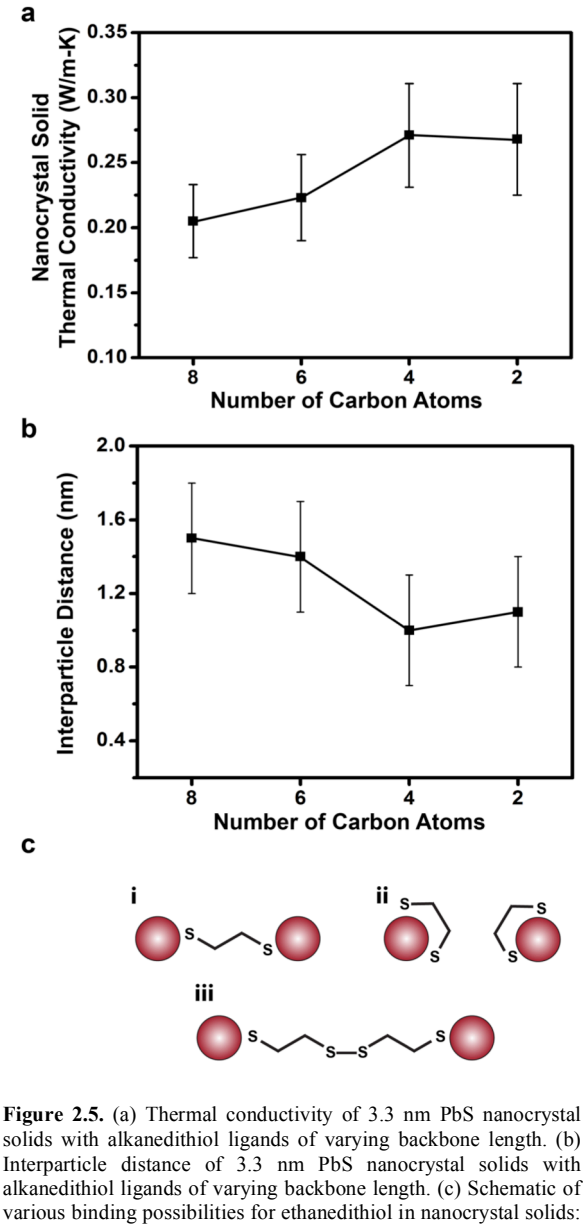

Figure 2.5. (a) Thermal conductivity of 3.3 nm PbS nanocrystal solids with alkanedithiol ligands of varying backbone length. (b) Interparticle distance of 3.3 nm PbS nanocrystal solids with alkanedithiol ligands of varying backbone length. (c) Schematic of various binding possibilities for ethanedithiol in nanocrystal solids: i. bridging, ii. bidentate, iii. dimerized.

find that PbS NC solids with EDA ligands have a higher thermal conductivity than with EDT ligands (Figure 2.4). This contrasts with data on SAM junctions, in which the thermal conductance through strong thiol-Au bonds is notably larger than the thermal conductance through weaker amine-Au bonds.[35] To expand upon this binding group motif, we also prepared PbS NC solids with halide ligands (Br^- and I^-). These ligands form ionic bonds to the NC surface, of which the PbS - Br^- bond is known to be the stronger of the two.[30] We find that the thermal conductivity of NC solids with these two ligands are essentially equivalent and do not reflect the prediction based on bond strength as well. Based on these experimental observations, we conclude that the thermal conductance of the NC core-ligand interface (*i.e.* the binding strength between the NC core and ligand) does not dominate thermal transport in NC solids. As based upon our EMA modeling (see below), we hypothesize that the ligand-ligand interface between neighboring NCs is the critical interface for thermal transport in NC solids.

We next study the effect of ligand length by using a series of alkanedithiol ligands with 2, 4, 6, and 8 carbon atoms (*i.e.* EDT, BDT, HDT, and ODT, respectively) on 3.3 nm PbS NC solids. As the ligand backbone decreased from 8 carbon atoms to 4 carbon atoms, the NC solid thermal conductivity increased from 0.20 W/m-K to 0.27 W/m-K (Figure 2.5a). We attribute this trend to a reduction of interparticle distance, which increases the NC core volume fraction in the solids. It is not surprising that this increases the thermal conductivity of the NC solid because the thermal conductivity of PbS is an order of magnitude higher than hydrocarbons.[39, 40] We also used x-ray reflectivity (XRR) to determine the mass densities of the NC solids with varying ligands, and then converted these values into interparticle distances using geometric arguments. We found that our interparticle distance measurements agree to within experimental uncertainty with much more sophisticated synchrotron x-ray scattering measurements.[25] Our interparticle distance trend shows an inverse correlation with our measured thermal

conductivities (Figures 2.5a and 2.5b), which supports our conclusion that interparticle distance is an important parameter affecting the thermal conductivity of NC solids. Interestingly, our results show no thermal conductivity increase as the ligand backbone is further reduced from 4 to 2 carbon atoms (BDT and EDT, respectively). While counterintuitive, we find that this thermal conductivity result still mirrors our findings on interparticle distance, which reveal approximately equivalent interparticle distances for BDT and EDT. We hypothesize that this change in trend for interparticle distance and thermal conductivity originates from a change in chemical binding motifs (Figure 2.5c). Similar property trend changes for varying alkanedithiol lengths have been observed in other works as well.[25, 33] Past studies have suggested that dithiol ligands preferentially bridge neighboring NCs (part i in Figure 2.5c).[25, 41, 42] Since our measured interparticle distances for NC solids with ODT, HDT, and BDT are comparable to that of the corresponding molecular lengths,[25] we hypothesize that NC bridging occurs in these cases. However, in the case of EDT, the interparticle distance is notably longer than the molecular length. This implies an alternative chemical binding motif; both bidentate binding[25, 33, 34] and dimerized binding[43, 44] (parts ii and iii, respectively, in Figure 2.5c) have been identified as possible binding arrangements for EDT in NC solids. We also performed XRR measurements on NC solids with EDA ligands and found very short interparticle distances (*i.e.* ~ 0.7 nm). This result suggests that EDA likely bridges NCs and provides an explanation as to why EDA ligands yield a higher NC solid thermal conductivity than EDT (Figure 2.4).

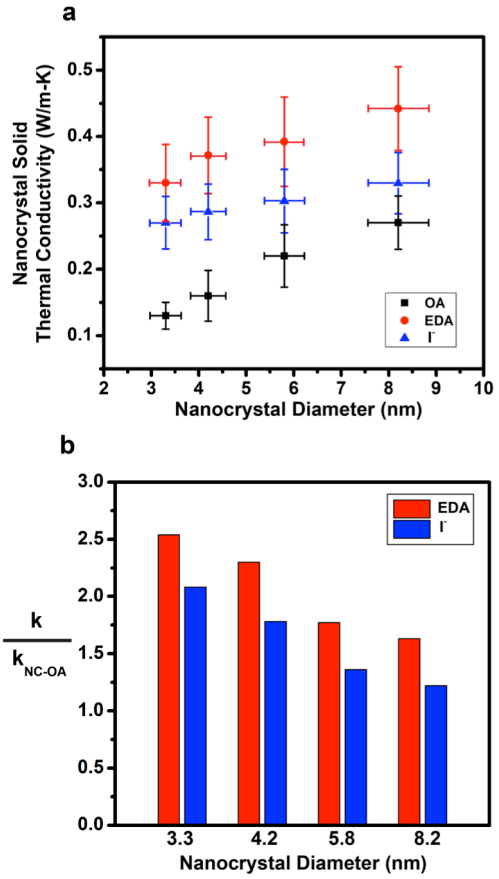

Figure 2.6. (a) The thermal conductivity of PbS nanocrystal solids with oleic acid (OA), ethylenediamine (EDA), and I^- ligands as a function of nanocrystal diameter. (b) The relative increase of thermal conductivity ($k/k_{NC\text{-}OA}$) in PbS nanocrystal solids with ethylenediamine (EDA) and I^- ligands and varying nanocrystal diameter. The data in part (b) is normalized to the thermal conductivity of PbS nanocrystal solids with OA ligands, $k_{NC\text{-}OA}$.

We next study the relative impact of surface chemistry on the thermal conductivity of NC solids with varying NC diameter. As a baseline, we first measure the thermal conductivity of PbS NC solids with their native OA ligands. We find that as the NC diameter increases from 3.3 to 8.2 nm, the thermal conductivity increases from 0.13 to 0.27 W/m-K, which agrees with measurements by Ong *et al.*[13] It is worth noting that our thermal conductivity measurements use the 3ω technique,[45-47] which is comparatively simpler to implement than Ong's frequency-domain thermal reflectance technique. This data demonstrates that nanocrystal solid thermal conductivity measurements should be accessible to a broader range of research labs. We next prepare each of these NC solids with I^- and EDA ligands and find that the thermal conductivity increases for all diameters (Figure 2.6a). This is consistent with the relationship between thermal conductivity and interparticle distance that we identified earlier. It is also possible that these ligand choices lead to higher effective thermal conductivities in the ligand matrix. In addition, we find that the relative thermal conductivity increase ($k/k_{NC\text{-}OA}$) is greater for smaller diameter NC solids than for larger diameters ones (Figure 2.6b). This trend is consistent with the fact that the ligands make up a greater volume fraction of the NC solid as the NC diameter decreases, and should therefore have a more substantial effect for smaller diameters. We achieve relative thermal conductivity increases of up to 150%, which improves upon the 50% increase demonstrated in prior work.[13] While data in prior work suggests that NC diameter is the parameter that most affects NC solid thermal conductivity,[13, 21, 22] our findings demonstrate that surface chemistry can have an even larger

impact. For example, consider the case of a 3.3 nm PbS NC solid with OA ligands, which has a thermal conductivity of 0.13 W/m-K. Increasing the NC diameter to 8.2 nm and keeping the native OA ligands leads to a thermal conductivity of 0.27 W/m-K. In contrast, keeping the same 3.3 nm diameter, but exchanging the OA with EDA leads to an even higher thermal conductivity of 0.33 W/m-K. Naturally, the effect of NC diameter and surface chemistry can be combined; we achieve our lowest thermal conductivity in 3.3 nm PbS with OA ligands and our highest thermal conductivity in 8.2 nm PbS with EDA ligands. Overall, we find that within our size range (~ 3-8 nm), the thermal conductivity of NC solids can be varied from approximately 0.1-0.4 W/m-K, which demonstrates a moderately larger range of possibilities than prior work.[13]

To gauge how this range of NC solid thermal conductivities can be further expanded, we use an EMA model to fit our data on PbS NCs with OA ligands and then perform a sensitivity analysis on the various model input parameters. Since thermal interface conductances significantly impact the thermal conductivity of nanocomposites, we incorporate this factor by using the EMA model proposed by Hasselman and Johnson.[48] This EMA model calculates the thermal conductivity of a composite by accounting for the constituent volume fractions, constituent thermal conductivities, and thermal interface conductance between the constituents. To apply the EMA model to our NC solid, we consider a nanocomposite consisting of NC cores in a ligand matrix. Figure 2.7a shows the EMA model fit to our PbS NC solids with OA ligands and varying diameter, which shows good agreement. In this fit we use 2 W/m-K, 0.13 W/m-K, 2.5 nm, and 220 MW/m^2-K for the NC core thermal conductivity (k_{NC}), ligand matrix thermal conductivity (k_m), interparticle distance, and NC core-ligand thermal interface conductance (G), respectively. Our choice of these input parameters for the model is based upon results in the literature.[13, 25, 35, 49]

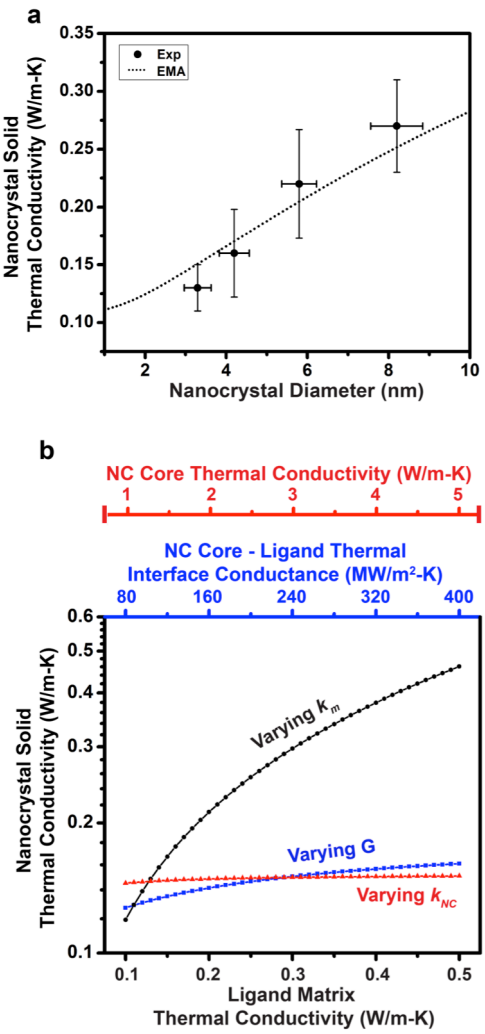

Figure 2.7. (a) Effective medium approximation (EMA) model results and corresponding experimental data for the thermal conductivity of PbS nanocrystal (NC) solids with oleic acid ligands and varying diameter. (b) Sensitivity analysis on the EMA model for 3.3 nm PbS NC solids with three independent parameters: NC core thermal conductivity (k_{NC}, red triangles), NC core-ligand interface thermal conductance (G, blue rectangles), and ligand matrix thermal conductivity (k_m, black spheres)

To study the relative impact of each parameter (k_{NC}, G, and k_m) on NC solid thermal conductivity, we independently vary each parameter while holding the other two constant (Figure 2.7b). We find that k_m has the largest impact, G has a moderate impact, and k_{NC} has a small impact. As k_m, G, and k_{NC} are each varied by a factor of 5, we calculate changes in NC solid thermal conductivity of 386%, 27%, and 4%, respectively. The insensitivity to k_{NC} is not surprising given that it is an order of magnitude larger than k_m and the core-ligand interfaces further restrict this thermal pathway. Prior experimental work has also found that NC solid thermal conductivity is largely independent of k_{NC}.[13] The fact that the NC solid thermal conductivity sensitivity is much greater to k_m than G means the thermal conductance of the ligand matrix is more important than the thermal conductance of the NC core-ligand interface. This possibly explains why we did not experimentally observe an increase in NC solid thermal conductivity as we increased the NC core-ligand binding strength (which, according to literature on solid-SAM junctions, should have increased the NC core-ligand thermal interface conductance). It is also worth noting that the thermal interface conductance of an individual solid-SAM interface only changes by about a factor of 4 as the solid-SAM

bond is changed from van der Waals to covalent.[35, 49] According to our EMA model, this would correspond to an ~ 20% change in NC thermal conductivity. Given that the NC core-ligand bond strength is varied in a much narrower range during our experiments, any thermal conductivity changes arising from NC core-ligand bond strength were likely small, which explains why our measurements did not detect significant changes.

Since k_m affects NC solid thermal conductivity the most, determining ways to increase or decrease k_m is a promising route to achieve an expanded thermal conductivity range beyond that demonstrated in the present work. It is notable that the maximum thermal conductivity for the matrix used in our EMA sensitivity analysis is only 0.5 W/m-K, which is comparable to typical thermal insulators. Consequently, there should be room to increase the thermal conductivity of the ligand matrix, and by extension, increase the thermal conductivity of the NC solid. This finding inspires us to hypothesize why thermal transport in the ligand matrix is poor to begin with. If we consider heat flow between two neighboring NCs, there are three interfaces: a NC core-ligand interface, a ligand-ligand interface, and then another NC core-ligand interface. Whereas the NC core-ligand interfaces are generally strong covalent or ionic bonds, the ligand-ligand interface is characterized by weak van der Waals forces. Several studies on polymers,[50] molecular crystals,[51] and carbon nanotube – polymer composites[52] have identified weak van der Waals interactions as rate-limiters for heat transfer. We hypothesize that this is also true for thermal transport in NC solids. We note that there is no analogous ligand-ligand interface in solid-SAM-solid structures, which may explain why the solid-molecule binding strength plays a significant thermal transport role in SAMs, but not necessarily in NC solids.

We hypothesize that two possible ways to increase the thermal conductivity of NC solids are (i) chemically crosslinking the NC ligands to strengthen the ligand-ligand interaction, (ii) eliminating the ligand-ligand interaction by bridging neighboring NCs with bifunctional ligands. The first concept has been demonstrated in a recent study on amorphous polymer blends; by introducing appropriately engineered crosslinkers, the thermal conductivity of the polymer blend was increased by a factor of 7.[53] The second approach has been highly sought after in studies to improve charge transport in NC solids,[42, 54, 55] and motivated our choice of bifunctional ligands (*e.g.* dithiols and diamine) in this study. However, this approach will likely prove complex because NC surfaces are highly curved, which leads to non-uniform distances between neighboring NCs. This curvature limits the surface area upon which ligand bridging can occur and may explain why we only observed moderately higher thermal conductivities with bridging ligands (*e.g.* EDA) relative to non-bridging ligands (*e.g.* EDT and I^-). Using colloidal nanocrystals with flat surfaces (*e.g.* cubes) and/or more sophisticated ligand chemistries that can achieve bridging throughout the entire NC surface could prove interesting.

2.4. Conclusion

We have systematically explored the effect of ligand length, ligand binding group, and NC diameter on thermal transport in colloidal PbS NC solids. The primary effect of decreasing ligand length and/or increasing NC diameter is to increase the NC solid thermal conductivity by decreasing the volume fraction of the thermally insulating ligand matrix. Varying the ligand binding strength to the NC core does not lead to significant effects on thermal transport, which contrasts with literature on solid-SAM-solid junctions. We find that the choice of ligands can affect the thermal conductivity by up to a factor of 2.5 and that the thermal conductivity of NC solids can be varied by an overall factor of 4, from ~ 0.1 to 0.4 W/m-K. By combining our experimental observations with EMA modeling, we identified the ligand-ligand interface between neighboring NCs as a critical interface for heat transfer. We then suggested ways to modify this interface and possibly increase NC solid thermal conductivity. Identifying ways to increase thermal conductivity will be beneficial to NC solid applications in electronics and optoelectronics, for which heat dissipation is important to device performance and lifetime. On the other hand, the naturally low thermal conductivities of NC solids bode well for NC solid-based thermoelectrics.

2.5. References for Section 2.

1. Llordes, A.; Garcia, G.; Gazquez, J.; Milliron, D. J. Tunable near-Infrared and Visible-Light Transmittance in Nanocrystal-in-Glass Composites. *Nature* **2013,** *500*, 323-326.
2. Wang, R. Y.; Feser, J. P.; Lee, J.-S.; Talapin, D. V.; Segalman, R.; Majumdar, A. Enhanced Thermopower in Pbse Nanocrystal Quantum Dot Superlattices. *Nano Lett.* **2008,** *8*, 2283-2288.
3. Liu, M.; Ma, Y.; Wu, H.; Wang, R. Y. Metal Matrix-Metal Nanoparticle Composites with Tunable Melting Temperature and High Thermal Conductivity for Phase-Change Thermal Storage. *ACS Nano* **2015,** *9*, 1341-1351.
4. Dai, X.; Zhang, Z.; Jin, Y.; Niu, Y.; Cao, H.; Liang, X.; Chen, L.; Wang, J.; Peng, X. Solution-Processed, High-Performance Light-Emitting Diodes Based on Quantum Dots. *Nature* **2014,** *515*, 96-99.
5. Cho, K. S.; Lee, E. K.; Joo, W. J.; Jang, E.; Kim, T. H.; Lee, S. J.; Kwon, S. J.; Han, J. Y.; Kim, B. K.; Choi, B. L.*, et al.* High-Performance Crosslinked Colloidal Quantum-Dot Light-Emitting Diodes. *Nat. Photonics* **2009,** *3*, 341-345.
6. Mcdonald, S. A.; Konstantatos, G.; Zhang, S.; Cyr, P. W.; Klem, E. J.; Levina, L.; Sargent, E. H. Solution-Processed PbS Quantum Dot Infrared Photodetectors and Photovoltaics. *Nat. Mater.* **2005,** *4*, 138-142.
7. Chuang, C.-H. M.; Brown, P. R.; Bulović, V.; Bawendi, M. G. Improved Performance and Stability in Quantum Dot Solar Cells through Band Alignment Engineering. *Nat. Mater.* **2014,** *13*, 796-801.
8. Oh, S. J.; Wang, Z.; Berry, N. E.; Choi, J.-H.; Zhao, T.; Gaulding, E. A.; Paik, T.; Lai, Y.; Murray, C. B.; Kagan, C. R. Engineering Charge Injection and Charge Transport for High Performance PbSe Nanocrystal Thin Film Devices and Circuits. *Nano Lett.* **2014,** *14*, 6210-6216.
9. Turk, M. E.; Choi, J.-H.; Oh, S. J.; Fafarman, A. T.; Diroll, B. T.; Murray, C. B.; Kagan, C. R.; Kikkawa, J. M. Gate-Induced Carrier Delocalization in Quantum Dot Field Effect Transistors. *Nano Lett.* **2014,** *14*, 5948-5952.
10. Liu, M.; Wang, R. Y. Phase Change Nanocomposites with Tunable Melting Temperature and Thermal Energy Storage Density. *Nanoscale* **2013,** *5*, 7234-7237.
11. Fan, F.-J.; Yu, B.; Wang, Y.-X.; Zhu, Y.-L.; Liu, X.-J.; Yu, S.-H.; Ren, Z. Colloidal Synthesis of $Cu_2CdSnSe_4$ Nanocrystals and Hot-Pressing to Enhance the Thermoelectric Figure-of-Merit. *J. Am. Chem. Soc.* **2011,** *133*, 15910-15913.
12. Fan, F.-J.; Wang, Y.-X.; Liu, X.-J.; Wu, L.; Yu, S.-H. Large-Scale Colloidal Synthesis of Non-Stoichiometric $Cu_2ZnSnSe4$ Nanocrystals for Thermoelectric Applications. *Adv. Mater.* **2012,** *24*, 6158-6163.
13. Ong, W.-L.; Rupich, S. M.; Talapin, D. V.; McGaughey, A. J. H.; Malen, J. A. Surface Chemistry Mediates Thermal Transport in Three-Dimensional Nanocrystal Arrays. *Nat. Mater.* **2013,** *12*, 410-415.
14. Smith, A. R.; Yoon, W.; Heuer, W. B.; Baril, S. I. M.; Boercker, J. E.; Tischler, J. G.; Foos, E. E. Effect of Ligand Structure on the Optical and Electronic Properties of Nanocrystalline PbSe Films. *J. Phy. Chem. C* **2012,** *116*, 6031-6037.
15. Lee, J.-S.; Kovalenko, M. V.; Huang, J.; Chung, D. S.; Talapin, D. V. Band-Like Transport, High Electron Mobility and High Photoconductivity in All-Inorganic Nanocrystal Arrays. *Nat. Nanotechnol.* **2011,** *6*, 348-352.
16. Tang, J.; Kemp, K. W.; Hoogland, S.; Jeong, K. S.; Liu, H.; Levina, L.; Furukawa, M.; Wang, X.; Debnath, R.; Cha, D. Colloidal-Quantum-Dot Photovoltaics Using Atomic-Ligand Passivation. *Nat. Mater.* **2011,** *10*, 765-771.
17. Sun, Y.; Fang, H.; Pan, L.; Han, M.; Xu, S.; Wang, X.; Xu, B.; Wu, Y. Impact of Surface-Bound Small Molecules on the Thermoelectric Property of Self-Assembled Ag_2Te Nanocrystal Thin Films. *Nano Lett.* **2015,** *15*, 3748-3756.
18. Kovalenko, M. V.; Scheele, M.; Talapin, D. V. Colloidal Nanocrystals with Molecular Metal Chalcogenide Surface Ligands. *Science* **2009,** *324*, 1417-1420.

19. Giansante, C.; Infante, I.; Fabiano, E.; Grisorio, R.; Suranna, G. P.; Gigli, G. "Darker-Than-Black" PbS Quantum Dots: Enhancing Optical Absorption of Colloidal Semiconductor Nanocrystals Via Short Conjugated Ligands. *J. Am. Chem. Soc.* **2015,** *137*, 1875-1886.
20. Gao, Y.; Aerts, M.; Sandeep, C. S. S.; Talgorn, E.; Savenije, T. J.; Kinge, S.; Siebbeles, L. D. A.; Houtepen, A. J. Photoconductivity of PbSe Quantum-Dot Solids: Dependence on Ligand Anchor Group and Length. *ACS Nano* **2012,** *6*, 9606-9614.
21. Zanjani, M. B.; Lukes, J. R. Phonon Dispersion and Thermal Conductivity of Nanocrystal Superlattices Using Three-Dimensional Atomistic Models. *J. Appl. Phys.* **2014,** *115*, 143515.
22. Ong, W.-L.; Majumdar, S.; Malen, J. A.; McGaughey, A. J. H. Coupling of Organic and Inorganic Vibrational States and Their Thermal Transport in Nanocrystal Arrays. *J. Phy. Chem. C* **2014,** *118*, 7288-7295.
23. Szendrei, K.; Cordella, F.; Kovalenko, M. V.; Böberl, M.; Hesser, G.; Yarema, M.; Jarzab, D.; Mikhnenko, O. V.; Gocalinska, A.; Saba, M.*, et al.* Solution-Processable near-Ir Photodetectors Based on Electron Transfer from PbS Nanocrystals to Fullerene Derivatives. *Adv. Mater.* **2009,** *21*, 683-687.
24. Gao, J.; Perkins, C. L.; Luther, J. M.; Hanna, M. C.; Chen, H.-Y.; Semonin, O. E.; Nozik, A. J.; Ellingson, R. J.; Beard, M. C. N-Type Transition Metal Oxide as a Hole Extraction Layer in PbS Quantum Dot Solar Cells. *Nano Lett.* **2011,** *11*, 3263-3266.
25. Weidman, M. C.; Yager, K. G.; Tisdale, W. A. Interparticle Spacing and Structural Ordering in Superlattice PbS Nanocrystal Solids Undergoing Ligand Exchange. *Chem. Mater.* **2015,** *27*, 474-482.
26. Zherebetskyy, D.; Scheele, M.; Zhang, Y.; Bronstein, N.; Thompson, C.; Britt, D.; Salmeron, M.; Alivisatos, P.; Wang, L.-W. Hydroxylation of the Surface of PbS Nanocrystals Passivated with Oleic Acid. *Science* **2014,** *344*, 1380-1384.
27. Podsiadlo, P.; Krylova, G.; Lee, B.; Critchley, K.; Gosztola, D. J.; Talapin, D. V.; Ashby, P. D.; Shevchenko, E. V. The Role of Order, Nanocrystal Size, and Capping Ligands in the Collective Mechanical Response of Three-Dimensional Nanocrystal Solids. *J. Am. Chem. Soc.* **2010,** *132*, 8953-8960.
28. Cademartiri, L.; Montanari, E.; Calestani, G.; Migliori, A.; Guagliardi, A.; Ozin, G. A. Size-Dependent Extinction Coefficients of PbS Quantum Dots. *J. Am. Chem. Soc.* **2006,** *128*, 10337-10346.
29. Konstantatos, G.; Howard, I.; Fischer, A.; Hoogland, S.; Clifford, J.; Klem, E.; Levina, L.; Sargent, E. H. Ultrasensitive Solution-Cast Quantum Dot Photodetectors. *Nature* **2006,** *442*, 180-183.
30. Brown, P. R.; Kim, D.; Lunt, R. R.; Zhao, N.; Bawendi, M. G.; Grossman, J. C.; Bulović, V. Energy Level Modification in Lead Sulfide Quantum Dot Thin Films through Ligand Exchange. *ACS Nano* **2014,** *8*, 5863-5872.
31. Hines, M. A.; Scholes, G. D. Colloidal PbS Nanocrystals with Size-Tunable near-Infrared Emission: Observation of Post-Synthesis Self-Narrowing of the Particle Size Distribution. *Adv. Mater.* **2003,** *15*, 1844-1849.
32. Ning, Z.; Voznyy, O.; Pan, J.; Hoogland, S.; Adinolfi, V.; Xu, J.; Li, M.; Kirmani, A. R.; Sun, J.-P.; Minor, J.*, et al.* Air-Stable N-Type Colloidal Quantum Dot Solids. *Nat Mater* **2014,** *13*, 822-828.
33. Lynch, J.; Kotiuga, M.; Doan-Nguyen, V. V. T.; Queen, W. L.; Forster, J. D.; Schlitz, R. A.; Murray, C. B.; Neaton, J. B.; Chabinyc, M. L.; Urban, J. J. Ligand Coupling Symmetry Correlates with Thermopower Enhancement in Small-Molecule/Nanocrystal Hybrid Materials. *ACS Nano* **2014,** *8*, 10528-10536.
34. Luther, J. M.; Law, M.; Song, Q.; Perkins, C. L.; Beard, M. C.; Nozik, A. J. Structural, Optical, and Electrical Properties of Self-Assembled Films of Pbse Nanocrystals Treated with 1,2-Ethanedithiol. *ACS Nano* **2008,** *2*, 271-280.
35. Losego, M. D.; Grady, M. E.; Sottos, N. R.; Cahill, D. G.; Braun, P. V. Effects of Chemical Bonding on Heat Transport across Interfaces. *Nat. Mater.* **2012,** *11*, 502-506.

36. O'Brien, P. J.; Shenogin, S.; Liu, J.; Chow, P. K.; Laurencin, D.; Mutin, P. H.; Yamaguchi, M.; Keblinski, P.; Ramanath, G. Bonding-Induced Thermal Conductance Enhancement at Inorganic Heterointerfaces Using nanomolecular Monolayers. *Nat. Mater.* **2013,** *12*, 118-122.
37. Love, J. C.; Estroff, L. A.; Kriebel, J. K.; Nuzzo, R. G.; Whitesides, G. M. Self-Assembled Monolayers of Thiolates on Metals as a Form of Nanotechnology. *Chem. Rev.* **2005,** *105*, 1103-1170.
38. Lee, S.-M.; Jun, Y.-W.; Cho, S.-N.; Cheon, J. Single-Crystalline Star-Shaped Nanocrystals and Their Evolution: Programming the Geometry of Nano-Building Blocks. *J. Am. Chem. Soc.* **2002,** *124*, 11244-11245.
39. Thermal Conductivity Graphs for C8 to C28 Compounds. In *Handbook of Thermal Conductivity*, Carl, L. Y., Ed. Gulf Professional Publishing: 1995; Vol. Volume 3, pp 1-363.
40. Skelton, J. M.; Parker, S. C.; Togo, A.; Tanaka, I.; Walsh, A. Thermal Physics of the Lead Chalcogenides PbS, PbSe, and PbTe from First Principles. *Phys. Rev. B* **2014,** *89*, 205203.
41. Talapin, D. V.; Lee, J.-S.; Kovalenko, M. V.; Shevchenko, E. V. Prospects of Colloidal Nanocrystals for Electronic and Optoelectronic Applications. *Chem. Rev.* **2010,** *110*, 389-458.
42. Koleilat, G. I.; Levina, L.; Shukla, H.; Myrskog, S. H.; Hinds, S.; Pattantyus-Abraham, A. G.; Sargent, E. H. Efficient, Stable Infrared Photovoltaics Based on Solution-Cast Colloidal Quantum Dots. *ACS Nano* **2008,** *2*, 833-840.
43. Joo, S. W.; Han, S. W.; Kim, K. Multilayer Formation of 1,2-Ethanedithiol on Gold: Surface-Enhanced Raman Scattering and Ellipsometry Study. *Langmuir* **2000,** *16*, 5391-5396.
44. Qu, D.; Kim, B.-C.; Lee, C.-W. J.; Uosaki, K. 1, N-Alkanedithiol (N= 2, 4, 6, 8, 10) Self-Assembled Monolayers on Au (111): Electrochemical and Theoretical Approach. *Bull. Korean Chem. Soc.* **2009,** *30*, 2549-2554.
45. Cahill, D. G. Thermal Conductivity Measurement from 30 to 750 K: The 3ω Method. *Rev. Sci. Instrum.* **1990,** *61*, 802-808.
46. Lee, S.-M.; Cahill, D. G. Heat Transport in Thin Dielectric Films. *J. Appl. Phys.* **1997,** *81*, 2590-2595.
47. Borca-Tasciuc, T.; Kumar, A. R.; Chen, G. Data Reduction in 3ω Method for Thin-Film Thermal Conductivity Determination. *Rev. Sci. Instrum.* **2001,** *72*, 2139-2147.
48. Hasselman, D.; Johnson, L. F. Effective Thermal Conductivity of Composites with Interfacial Thermal Barrier Resistance. *J. Compos. Mater.* **1987,** *21*, 508-515.
49. Wang, Z.; Carter, J. A.; Lagutchev, A.; Koh, Y. K.; Seong, N.-H.; Cahill, D. G.; Dlott, D. D. Ultrafast Flash Thermal Conductance of Molecular Chains. *Science* **2007,** *317*, 787-790.
50. Shen, S.; Henry, A.; Tong, J.; Zheng, R.; Chen, G. Polyethylene Nanofibres with Very High Thermal Conductivities. *Nat. Nanotechnol.* **2010,** *5*, 251-255.
51. Andersson, O.; Soldatov, A.; Sundqvist, B. Thermal Conductivity of C60 at Pressures up to 1 Gpa and Temperatures in the 50 to 300 K Range. *Phys. Rev. B* **1996,** *54*, 3093-3100.
52. Marconnett, A. M.; Yamamoto, N.; Panzer, M. A.; Wardle, B. L.; Goodson, K. E. Thermal Conduction in Aligned Carbon Nanotube-Polymer Nanocomposites with High Packing Density. *ACS Nano* **2011,** *5*, 4818-4825.
53. Kim, G.-H.; Lee, D.; Shanker, A.; Shao, L.; Kwon, M. S.; Gidley, D.; Kim, J.; Pipe, K. P. High Thermal Conductivity in Amorphous Polymer Blends by Engineered Interchain Interactions. *Nat. Mater.* **2015,** *14*, 295-300.
54. Yu, D.; Wang, C.; Guyot-Sionnest, P. N-Type Conducting Cdse Nanocrystal Solids. *Science* **2003,** *300*, 1277-1280.
55. Müller, K. H.; Wei, G.; Raguse, B.; Myers, J. Three-Dimensional Percolation Effect on Electrical Conductivity in Films of Metal Nanoparticles Linked by Organic Molecules. *Phys. Rev. B* **2003,** *68*, 155407.

3.0. Colloidal Nanocrystal Superlattices as Phononic Crystals: Plane Wave Expansion Modeling of Phonon Band Structure

3.1. Introduction

Phonons are vibrational waves that transport sound and heat.[1] The phononic band diagram (also known as the dispersion relationship) relates the frequency of a given phonon to its corresponding wave vector and is analogous to electronic and photonic band diagrams. By exercising control over the phonon band structure, it is possible to manipulate the transport of sound and heat. One common method of engineering band structure is to create phononic crystals, which are artificially made materials with periodic variations in acoustic impedance (e.g. alternating hard and soft materials). This periodicity results in a phononic band gap that forbids the propagation of phonons in a particular frequency range.[2-5] The phononic crystal is the vibrational wave analogue to the well-known photonic crystal, which uses periodic variations in refractive index to create a photonic band gap.[6, 7] Two key characteristics of a phononic band gap are its center frequency and its width. The band gap fundamentally arises from wave interference, which requires that the periodicity be comparable to the phonon wavelength; hence shorter periodicities lead to phononic band gaps with higher center frequencies. The width of the phononic band gap depends on the acoustic impedance ratio of the phononic crystal's components; the further this ratio deviates from unity, the wider the band gap.[2] Hence a phononic crystal made of alternating hard and soft materials will have a wider band gap than one made of two alternating hard materials. Depending on the number of dimensions in which periodicity occurs, phononic crystals are described as 1-, 2-, or 3-dimensional (i.e. periodic planes, cylinders, and spheres, respectively). Phononic crystals are a promising class of materials for sound and heat manipulation and have been used to create phonon waveguides, cavities, filters, sensors, switches and rectifiers.[8-14]

Phononic crystals are commonly constructed through the assembly of macroscopic building blocks or top-down fabrication methods such as lithography.[15-17] These fabrication approaches have yielded phononic band gaps with center frequencies in the ~ 1 kHz – 10 GHz frequency range. Extending this center frequency range above 10 GHz is desirable because such structures can potentially manipulate heat conduction[14, 18, 19] and/or enable novel optomechanical devices.[20-23] Creating phononic band gaps in this frequency range generally requires nanostructured materials with periodicities of $\lesssim$ 10 nm. While 1-dimensional phononic crystals made via sequential thin film deposition have achieved band gaps in this frequency range,[24, 25] creating 3-dimensional periodicities on this length scale is much more difficult. Phononic band gaps with center frequencies above 10 GHz have yet to be experimentally observed in 3-dimensional phononic crystals.[26, 27]

In this work, we suggest that colloidal nanocrystals can form a natural basis for the bottom-up assembly of 3-dimensional phononic crystals with record high frequency band gaps. Colloidal nanocrystals consist of an inorganic crystalline core with organic ligands (e.g. oleic acid, alkanethiols, etc.) bound to the surface (Figure 3.1a). Elegant precision and control over colloidal nanocrystal size, shape, and composition has now become commonplace and is summarized in a number of reviews.[28-31] Colloidal nanocrystal-based materials have received attention for a wide range of applications spanning photovoltaics,[32, 33] light-emitting diodes,[34, 35] thermoelectrics,[36-38] thermal storage,[39-41] and electronics.[42, 43] In contrast, the use of colloidal nanocrystals for phononic crystals has received very limited attention.[44, 45] The diameter of a colloidal nanocrystal core is typically controlled to be between ~ 2 – 15 nm, which overlaps nicely with the necessary length-scales needed to achieve phononic band gaps in the 10^1 – 10^2 GHz frequency range. In addition, van der Waals interactions between the nanocrystal ligand molecules facilitate the self-assembly of colloidal nanocrystals into periodic three-dimensional arrays.[46, 47] Analogous to the atomic lattice of a crystal, the colloidal nanocrystal community refers to these assemblies as "nanocrystal

superlattices." These superlattices are a natural choice for phononic crystals because their periodic nanocrystal cores and ligand matrix can function as the two components of a phononic crystal (Figure 3.1b). In addition to having high band gap center frequencies due to small-scale periodicity, colloidal nanocrystal superlattices should also have wide band gaps due to the acoustic contrast between the hard inorganic nanocrystal cores and the soft ligand matrix.

In this work, we use plane wave expansion (PWE) techniques to model the phonon band structure of colloidal nanocrystal superlattices and explore their potential as phononic crystals. Our modeling demonstrates that superlattices can have phononic band gaps with center frequencies on the order of ~ 10^2 GHz and band gap widths on the order of ~ 10^1 GHz. We also systematically vary nanocrystal core diameter, d, nanocrystal core elastic modulus, E_{NC}, interparticle distance (i.e., ligand length), L, and ligand elastic modulus, E_{ligand}, and report on the corresponding effects on the phonon band structure. Our modeling shows that the band gap center frequency increases as the d and L are decreased, or as $E_{NC\ Core}$ and E_{ligand} are increased. The band gap width behaves non-monotonically with d, L, $E_{NC\ Core}$, and E_{ligand}, and intercoupling of these variables can eliminate the band gap. Lastly, we observe multiple phononic band gaps in many superlattices and find a correlation between an increase in the number of band gaps and increases in d and $E_{NC\ Core}$. We find that increases in the property mismatch between phononic crystal components (i.e., d/L and $E_{NC\ Core}/E_{ligand}$) flattens the phonon branches and is a key driver in increasing the number of phononic band gaps.

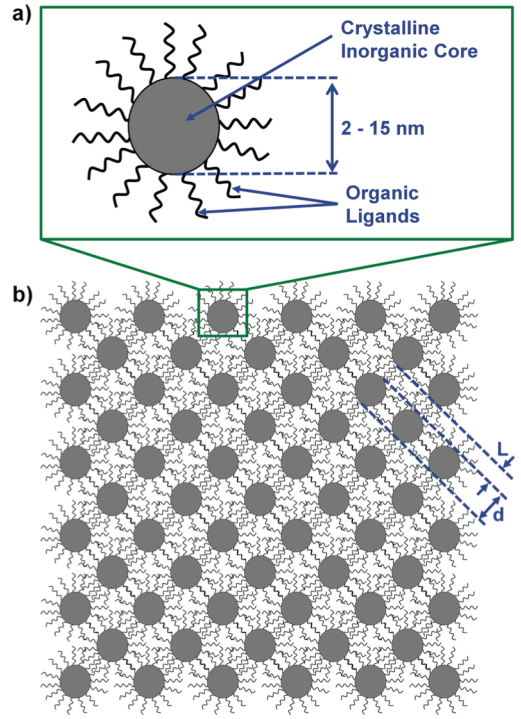

Figure 3.1. Schematics of (a) an individual colloidal nanocrystal and (b) a face-centered cubic colloidal nanocrystal superlattice as viewed along the [100] direction. An individual colloidal nanocrystal consists of a crystalline inorganic core with organic ligands on its surface (e.g. oleic acid, alkanethiols, etc.). When colloidal nanocrystals are assembled into a superlattice, they form a phononic crystal that consists of a periodic array of hard nanocrystal cores embedded in a soft ligand matrix. The two key length scales in the phononic crystal are the diameter of the inorganic nanocrystal core, d, and the interparticle distance, L. The interparticle distance is primarily determined by the ligand length.

3.2. Methodology

Calculating the phonon band structure requires solving for the phononic crystal's normal modes of vibration and determining their corresponding characteristic frequencies. This is often accomplished using finite difference time domain methods,[48-50] finite element methods,[45, 51, 52] plane wave expansion (PWE) methods,[53-55] and combined molecular dynamics - lattice dynamics approaches.[44, 56, 57] We utilize the PWE method to determine the phonon band structure in this paper. The PWE method's chief strength is that in-house codes that are computationally inexpensive and adaptable to parallel computation can be written with relative ease. This enables users to achieve maximum control over their computational goals. While many commercial finite element method packages are available, computational flexibility is lost when using these packages. Although molecular dynamics and finite difference time domain methods are also powerful approaches, they suffer from being computationally expensive.

In the PWE method, the elastic wave equation is converted into an eigenvalue/eigenvector problem by utilizing the periodicity of the lattice and Bloch's theorem.[58] Since the eigenvectors and eigenvalues correspond to the phonon wave vectors, $\boldsymbol{k}$, and angular frequencies, ω, the PWE method directly yields the phonon band diagram. Our implementation of the PWE method follows

the procedure described by Economou and Sigalas.[53, 59] We begin with the elastic wave equation in three dimensions for a locally isotropic medium:

$$\frac{\partial^2 u^i}{\partial t^2} = \frac{1}{\rho}\left[\frac{\partial}{\partial x_i}\left(\lambda \frac{\partial u^l}{\partial x_l}\right) + \frac{\partial}{\partial x_l}\left(\mu\left[\frac{\partial u^i}{\partial x_l} + \frac{\partial u^l}{\partial x_i}\right]\right)\right] \quad (1)$$

where t is time, i and l are indices (1, 2, or 3), and u^i, u^l, x_i and x_l are the Cartesian components of the displacement vector, $\boldsymbol{u}(\boldsymbol{r})$, and position vector, $\boldsymbol{r}$, respectively. The spatially varying density, first Lamé coefficient, and second Lamé coefficient are represented by $\rho(\boldsymbol{r})$, $\lambda(\boldsymbol{r})$ and $\mu(\boldsymbol{r})$, respectively. Since phononic crystals are periodic, the local material properties are also periodic and can be expressed using a spatial Fourier series for the primitive unit cell.

$$\rho(\boldsymbol{r}) = \sum_{\boldsymbol{G}} \rho_{\boldsymbol{G}} e^{j\boldsymbol{G}\cdot\boldsymbol{r}} \quad (2a)$$
$$\lambda(\boldsymbol{r}) = \sum_{\boldsymbol{G}} \lambda_{\boldsymbol{G}} e^{j\boldsymbol{G}\cdot\boldsymbol{r}} \quad (2b)$$
$$\mu(\boldsymbol{r}) = \sum_{\boldsymbol{G}} \mu_{\boldsymbol{G}} e^{j\boldsymbol{G}\cdot\boldsymbol{r}} \quad (2c)$$

where $\boldsymbol{G}$ is a reciprocal lattice vector, j is the imaginary unit, and subscript $\boldsymbol{G}$ refers to the $\boldsymbol{G}$th Fourier component of the indicated property. Since all of the coefficients in the elastic wave equation are periodic, we can employ Bloch's theorem to write:

$$\boldsymbol{u}(\boldsymbol{r}) = u_{\boldsymbol{k}}(\boldsymbol{r}) e^{j\boldsymbol{k}\cdot\boldsymbol{r}} = \sum_{\boldsymbol{G}} u_{\boldsymbol{k}+\boldsymbol{G}}\, e^{j(\boldsymbol{k}+\boldsymbol{G})\cdot\boldsymbol{r}} \quad (3)$$

which has plane wave solutions in the form of:

$$u = e^{j(\boldsymbol{k}\cdot\boldsymbol{r}-\omega t)} \quad (4)$$

Equations 1 – 4 can be combined to yield the following eigenvalue problem:[53]

$$\omega^2 u^i_{\boldsymbol{k_0}+\boldsymbol{G}} = \sum_{\boldsymbol{G}'}\left[\sum_{l,\boldsymbol{G}} \rho^{-1}_{\boldsymbol{G}-\boldsymbol{G}''}\left[\lambda_{\boldsymbol{G}''-\boldsymbol{G}'}(\boldsymbol{k_0}+\boldsymbol{G}')_l(\boldsymbol{k_0}+\boldsymbol{G}'')_i + \mu_{\boldsymbol{G}''-\boldsymbol{G}'}(\boldsymbol{k_0}+\boldsymbol{G}')_i(\boldsymbol{k_0}+\boldsymbol{G}'')_l\right]u^l_{\boldsymbol{k_0}+\boldsymbol{G}'} + \sum_{\boldsymbol{G}''}\left(\rho^{-1}_{\boldsymbol{G}-\boldsymbol{G}''}\,\mu_{\boldsymbol{G}''-\boldsymbol{G}'}\sum_n(\boldsymbol{k_0}+\boldsymbol{G}')_n(\boldsymbol{k_0}+\boldsymbol{G}'')_n\right)u^i_{\boldsymbol{k_0}+\boldsymbol{G}'}\right] \quad (5)$$

where $\boldsymbol{k_o}$ is a wave vector, $\boldsymbol{G}, \boldsymbol{G}'$ and $\boldsymbol{G}''$ are reciprocal lattice vectors, and i, l, and n are indices that vary between 1, 2, and 3. If the dimensions and mechanical properties of a phononic crystal's constituent phases are specified, Equation 5 can be rewritten in matrix form and solved to obtain the eigenfrequencies, ω, of the eigenvector, $\boldsymbol{k_o}$. Varying $\boldsymbol{k_o}$ throughout the Brillouin zone then allows the phonon band diagram to be mapped out. Whereas the above equations are written in terms of λ and μ, experimental measurements on the mechanical properties of nanocrystal superlattices have generally been reported in terms of the bulk modulus, B, and elastic modulus, E.[60-62] If Poisson's ratio, ν, is known, then bulk moduli can be converted into elastic moduli. In addition, the mechanical property set of E and υ can be transformed into λ and μ via the following relations:[63]

$$\mu = \frac{E}{2(1+\nu)} \quad (6a)$$
$$\lambda = \frac{\nu \times E}{((1+\nu)\times(1-2\nu))} \quad (6b)$$

To apply the PWE method to colloidal nanocrystal superlattices we consider the nanocrystal cores and nanocrystal ligands as the two components of a phononic crystal (i.e. a periodic arrangement of inorganic spheres embedded in ligand matrix). We focus our modeling effort on face-centered-cubic lattices because this is the arrangement that colloidal nanocrystal superlattices most commonly adopt.[61] Figure 3.2 illustrates the conventional unit cell, primitive unit cell, and first Brillouin zone of a face-centered cubic lattice with nanocrystal diameter, d, interparticle distance, L, and lattice constant, a.

Of the many varieties of colloidal nanocrystal superlattices, the most complete set of experimentally measured mechanical properties correspond to superlattices consisting of PbS nanocrystals with oleic acid ligands.[60-62] Consequently we initiate our phonon band diagram discussion on this particular superlattice (Figure 3.3), and use input values of interparticle distance, L = 1.5 nm, nanocrystal core elastic modulus, $E_{NC\ core}$ = 54 GPa, ligand matrix elastic modulus, E_{ligand} = 2.6 GPa, nanocrystal core density, $\rho_{NC\ core}$ = 7600 kg/m^3, ligand matrix density, ρ_{ligand} = 895 kg/m^3, nanocrystal core Poisson's ratio, $\nu_{NC\ core}$ = 1/3, and ligand matrix Poisson's ratio, ν_{ligand} = 1/3. Unless otherwise stated, these parameters are used in all of this paper's calculations.

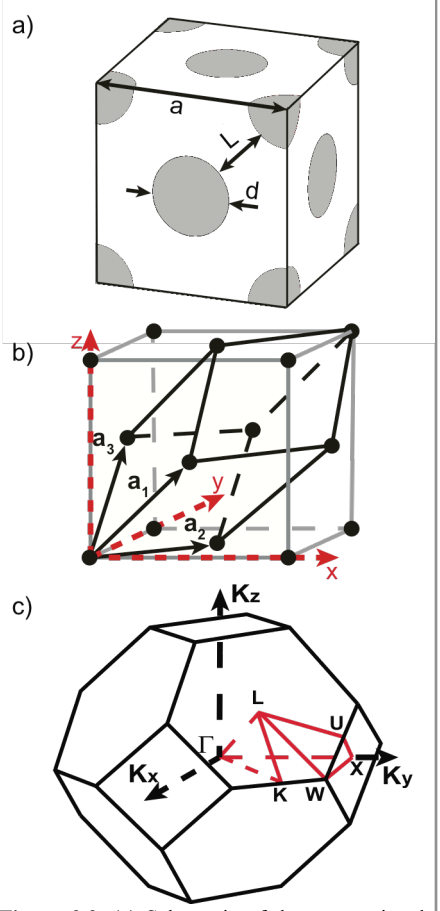

Figure 3.2. (a) Schematic of the conventional unit cell for a face-centered cubic lattice with relevant geometrical parameters labeled: interparticle distance, L, lattice constant, a, and nanocrystal core diameter, d. (b) Schematic of a primitive unit cell for a face-centered cubic lattice and corresponding primitive lattice vectors, $\boldsymbol{a}_1$, $\boldsymbol{a}_2$, and $\boldsymbol{a}_3$. (c) Schematic of the first Brillouin zone (black lines) and the irreducible region of the first Brillouin zone (red lines).

Since the PWE method assumes that the phonon medium can be treated as a continuum, there is a maximum frequency and minimum length scale for which it is valid. Past studies have shown that continuum methods can reasonably predict phonon band structures up to a frequency of ~ 1 THz.[64, 65] To stay well below this threshold, we limit our model to frequencies ≤ 500 GHz. Furthermore, the shortest phonon wavelength considered in our calculations is 37.9 Å (this corresponds to the W point in the Brillouin zone for a nanocrystal core diameter of 2 nm and interparticle distance of 1 nm). This phonon wavelength is an order of magnitude larger than typical interatomic distances and represents a reasonable threshold for applying continuum approximations. Our use of the elastic wave equation implicitly assumes that the mechanical response of the material is within the linear regime, which means that our model only considers small vibrational wave amplitudes. The PWE method also uses periodic boundary conditions, which is equivalent to having perfect superlattice order. The primary effect of superlattice disorder would be to introduce phonon scattering sites and/or localized phonons (i.e. phonons that are not plane waves) that are not captured in the band diagram. In addition to the physical approximations of our methodology, numerical accuracy of our code is also important. To confirm our accuracy, we have checked it for computational convergence and benchmarked it against other PWE results in the literature.

3.3. Results and Discussion

Figure 3.3 shows the phonon band diagram for a superlattice consisting of PbS nanocrystals with oleic acid ligands and illustrates that these materials can have wide phononic band gaps with center frequencies in the 100 GHz-range. Phononic crystals with 3-dimensional periodicity

commonly have band gaps that exist only along particular crystallographic directions. A band gap that exists in every direction is less common and is referred to as an "absolute" or "complete" band gap.[66] Figure 3.3 shows that the PbS nanocrystal – oleic acid ligand superlattice exhibits this less common feature. The phonon branches that intersect the Γ point at the origin are known as "acoustic" branches whereas those that intersect the Γ point at non-zero frequency are known as "optical" branches. These branches appear in groups of three due to the three mechanical degrees of freedom. In typical atomic crystals (e.g. bulk GaP, AlAs, GaSb, etc.), the band gap commonly resides in between the acoustic phonon branches and the first set of optical branches. In contrast, the phononic band gap in the nanocrystal superlattice falls in between the first and second set of optical branches. Accompanying this band gap characteristic is a strong frequency overlap between the first set of optical phonon branches and the acoustic branches. This frequency overlap creates a large phase space for phonon-phonon scattering processes that satisfy scattering selection rules (i.e., conservations of energy and crystal momentum). This large phase space in turn creates opportunities for fast energy transfer between acoustic and optical phonons. Furthermore, since optical phonons interact with light and acoustic phonons do not, this frequency resonance between the optical and acoustic phonons suggests that fast energy transfer between photons and acoustic phonons can occur in nanocrystal superlattices.

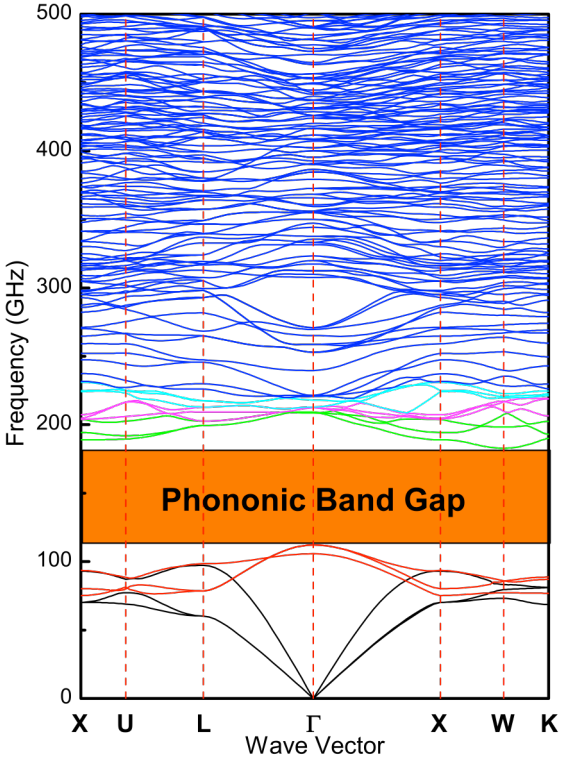

Figure 3.3. Phononic band diagram of a face-centered cubic colloidal nanocrystal superlattice comprised of PbS nanocrystals (E = 54 GPa, ν = 1/3, and ρ = 7600 kg/m^3) with oleic acid ligands (E = 2.6 GPa, ν = 1/3, and ρ = 895 kg/m^3). The nanocrystal core diameter and interparticle distance in this band diagram are d = 5 nm and L = 1.5 nm. To improve clarity, the first 5 sets of branches (i.e., 15 branches) are color-coded. The three acoustic branches are black, the first set of optical branches are red, the second set of optical branches are green, and subsequent sets of optical branches are purple and cyan, respectively.

We next discuss the effect of changing the nanocrystal core diameter, interparticle distance, and colloidal nanocrystal mechanical properties on the phonon band structure. In principle, there are eight phononic crystal variables, d, L, $E_{NC\ core}$, E_{ligand}, $\rho_{NC\ core}$, ρ_{ligand}, $\nu_{NC\ core}$, and ν_{ligand}. We vary the nanocrystal core through a typical colloidal nanocrystal diameter range of 2 – 15 nm. The interparticle distance in a nanocrystal superlattice is controlled by the organic ligands on the nanocrystal core surface. These ligands are typically small organic molecules such as oleic acid and alkanethiols. Consequently we vary the interparticle distance and matrix elastic modulus from 1 – 3 nm and 1 – 8 GPa, respectively, which are ranges that are representative of typical organic ligands. Since a very wide variety of nanocrystal core compositions are possible,[28-31] we vary the elastic modulus of the nanocrystal core over a large range of 10 – 1250 GPa. We found that varying Poisson's ratio had only a minor effect on the phononic band gap characteristics, and we therefore leave out discussion of this parameter. Inspection of Equations 5 and 6 reveal that density only shows up as a denominator for the elastic modulus and Poisson's ratio (i.e. E/ρ and ν/ρ). Since Poisson's ratio has only a minor effect on the band gap characteristics, the effect of varying density can be inferred by rescaling our results for varying elastic modulus. Phononic crystals are often described in terms of their volume fraction of matrix inclusions, which in our case corresponds to the nanocrystal core volume fraction. Since our calculations vary both

nanocrystal core diameter and interparticle distance (which is directly related to ligand length, see Figure 3.1), our calculations implicitly span a nanocrystal core volume fraction range of 4.7% to 61.0%. Lastly, we note that in some cases we observe multiple phononic band gaps were observed (see below); however, the most prominent band gap is the gap occurring between the first and second set of optical branches. Unless otherwise stated, the following discussion focuses on this band gap.

Figures 3.4a shows that decreasing the nanoparticle diameter and/or interparticle distance increases the center frequency of the band gap. This behavior arises because the center frequencies of phononic band gaps correspond to wavelengths that satisfy the Bragg condition (i.e., constructive interference of scattered waves from a periodic medium). Decreasing the nanoparticle diameter and/or interparticle distance decreases the unit cell length, which decreases the Bragg wavelength and increases the center frequency. The impact of changing interparticle distance on the center frequency is most pronounced at smaller nanoparticle diameters. This is because interparticle distance changes lead to large relative changes in unit cell sizes in this diameter regime. For large nanoparticle diameters, the effect of interparticle distance on center frequency is small because the unit cell size is dominated by the nanoparticle diameter. The band gap width can go to zero when combining small nanocrystal diameters with large interparticle distances and so we do not plot center frequencies in these instances (Figure 3.4a).

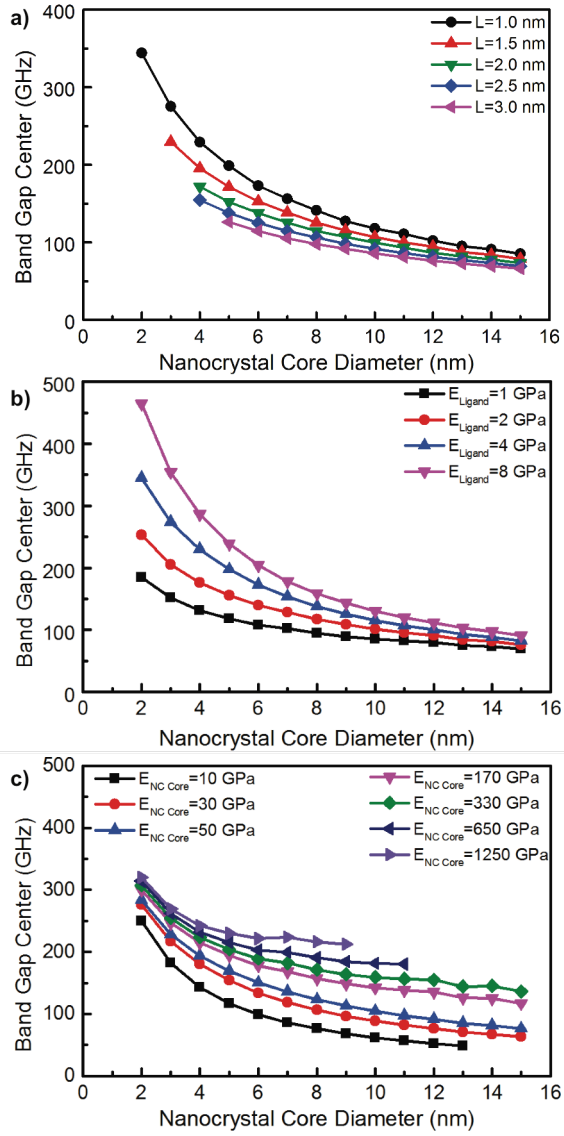

Figure 3.4. The effect of nanocrystal core diameter on the center frequency of the phononic band gap for: (a) varying interparticle distance, L; (b) varying elastic modulus of the ligand matrix, E_{ligand}; and (c) varying elastic modulus of the nanocrystal core, $E_{NC\ Core}$. Unless otherwise specified, L, E_{ligand}, and $E_{NC\ Core}$ are fixed at 1.5 nm, 2.6 GPa, and 54 GPa, respectively.

As the elastic modulus of the ligand matrix or nanocrystal core is increased, the center frequency of the phononic band gap increases monotonically (Figure 3.4b and 3.4c). Although the band gap center frequency increases in all cases, the magnitude of this increase is size dependent and depends on whether the modulus of the nanocrystal core or ligand matrix is changing. The ligand modulus has the greatest impact on the band gap center frequency at small nanoparticle diameters (Figure 3.4b). This is intuitive because the ligands make up the greatest fraction of the unit cell when the nanoparticle diameters are small. Analogously, the nanocrystal core modulus has the greatest impact at large nanoparticle diameters because this is when the nanocrystal cores make up the largest fraction of the unit cell (Figure 3.4c). Notably the band gap disappears at large diameters when the nanocrystal core modulus is very soft or very hard. For example, we do not observe band gaps above 9 and 13 nm diameters for nanocrystal core moduli of 1250 and 10 GPa, respectively.

The acoustic contrast between the soft ligand matrix and hard nanocrystal cores leads to large band gap widths of up to ~ 130 GHz for 2 nm diameters and 1 nm interparticle distances (Figure 3.5a). Interestingly, we observe a non-monotonic relationship between band gap width and nanoparticle diameter. The band gap width first rises with increasing diameter, reaches a maximum value at a critical diameter, d_{crit}, and then decreases. One implication of this non-monotonic behavior is that not all colloidal nanocrystal superlattices will have phononic band gaps. For example, our model predicts the absence of a phononic band gap for nanocrystal diameters below 4 nm with an interparticle distance of 3.0 nm.

The combined effects of d, L, E_{ligand}, and $E_{NC\ core}$ on phononic band gap width can be visualized in Figures 3.5a, 3.5b, and 3.5c. These figures collectively reveal an intricate and rich behavior between these parameters and phononic band gap width. This behavior is best visualized in Figure 3.5c, which shows the relationship between phononic band gap width and nanocrystal core diameter for a large range of $E_{NC\ core}$, 10 – 1250 GPa. In addition to an increasing band gap width below d_{crit} and a decreasing band gap width above d_{crit}, a second non-monotonic behavior is observed in Figure 3.5c. For nanocrystal core diameters 4 nm and larger, we see that the band gap width first increases with increasing $E_{NC\ Core}$, reaches a maximum, and then decreases with increasing $E_{NC\ Core}$. For example, nanocrystal core diameters of 8 nm have an increasing band gap width for 10 GPa < $E_{NC\ Core}$ < 170 GPa and decreasing band gap width for 170 GPa < $E_{NC\ Core}$ < 1250 GPa. This behavior causes the right sides of the curves in Figure 3.5c to first sweep diagonally up and then sweep diagonally down as $E_{NC\ Core}$ is changed from 10 to 1250 GPa. A similar, but subtler behavior can be seen in Figures 3.5a and 3.5b. The subtlety of this behavior for changes in L and E_{ligand} in Figure 3.5 arises because these parameters span a more narrow range than $E_{NC\ Core}$.

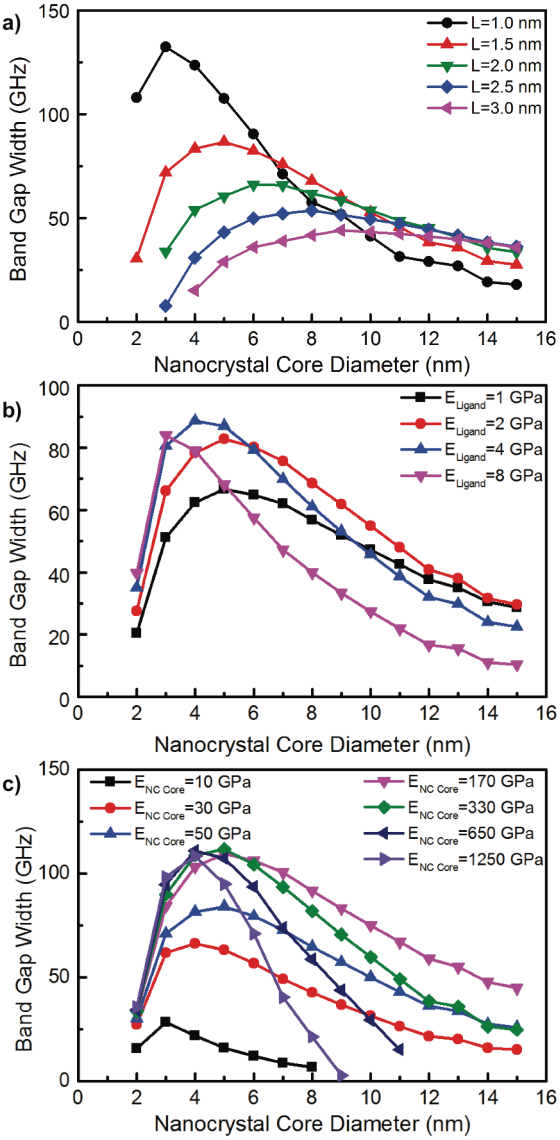

Figure 3.5. The effect of nanocrystal core diameter on the phononic band gap width for: (a) varying interparticle distance, L; (b) varying elastic modulus of the ligand matrix, E_{ligand}; and (c) varying elastic modulus of the nanocrystal core, $E_{NC\ Core}$. Unless otherwise specified, L, E_{ligand}, and $E_{NC\ Core}$ are fixed at 1.5 nm, 2.6 GPa, and 54 GPa, respectively.

The fact that band gap width increases, reaches a maximum, and then decreases as d, L, E_{ligand}, and $E_{NC\ core}$ are varied suggests that these four parameters impact band gap width in similar manners. This type of behavior has also been observed by Zanjani and Lukes,[45] who found that as interparticle distance increased, the phononic band gap width increased, reached a maximum, and then decreased. They explained the origin of this behavior by studying the Bragg frequencies of each phononic crystal component and utilizing a transfer matrix model. Their modeling found that as the Bragg frequency mismatch between the two components increased, the band gap first widened, then reached a maximum at moderate Bragg frequency separation, and then narrowed.

Since Bragg frequency is proportional to the square root of elastic modulus and inversely proportional to length, this Bragg frequency explanation can also explain our observed effects of elastic modulus on phononic band gap width. The four parameters varied in Figure 3.5, d, L, $E_{ligand,}$ and $E_{NC\ core}$, all have similar effects on the band gap width because each parameter has a role in determining the overall Bragg frequency mismatch between the nanocrystal cores and ligand matrix. In effect, the band gap width data in Figure 3.5 represents slices of a surface in a 4-dimensional space (i.e. d, L, $E_{ligand,}$ and $E_{NC\ core}$).

In many instances, we observe multiple band gaps in the phonon band diagram (Figures 3.6 and 7). The band gap between the first and second set of optical branches tends to be the widest and higher frequency band gaps tend to be much more narrow. Our data also shows a correlation between increases in nanocrystal core diameter and the number of band gaps (Figures 3.6a and 3.6c) and increases in the nanocrystal core elastic modulus and the number of band gaps (Figures 3.6b and 3.6d). The origins of these correlations can be explained by observing the band diagram characteristics for changes in nanocrystal core diameter (Figures 3.7a – 3.7c) and nanocrystal core elastic modulus (Figures 3.7d – 3.7f). It is well known that increasing property mismatches causes flattening of the phonon dispersion branches.[67] The effects of increasing nanocrystal core diameter and increasing nanocrystal core elastic modulus are to increase mismatch with the ligand matrix (i.e. d / L and $E_{NC\ core}$ / E_{ligand} increase). As the phonon branches flatten, this leads to more opportunities to form phononic band gaps and hence we observe a correlation between an increase in the number of band gaps and an increase in nanocrystal core diameter and elastic modulus.

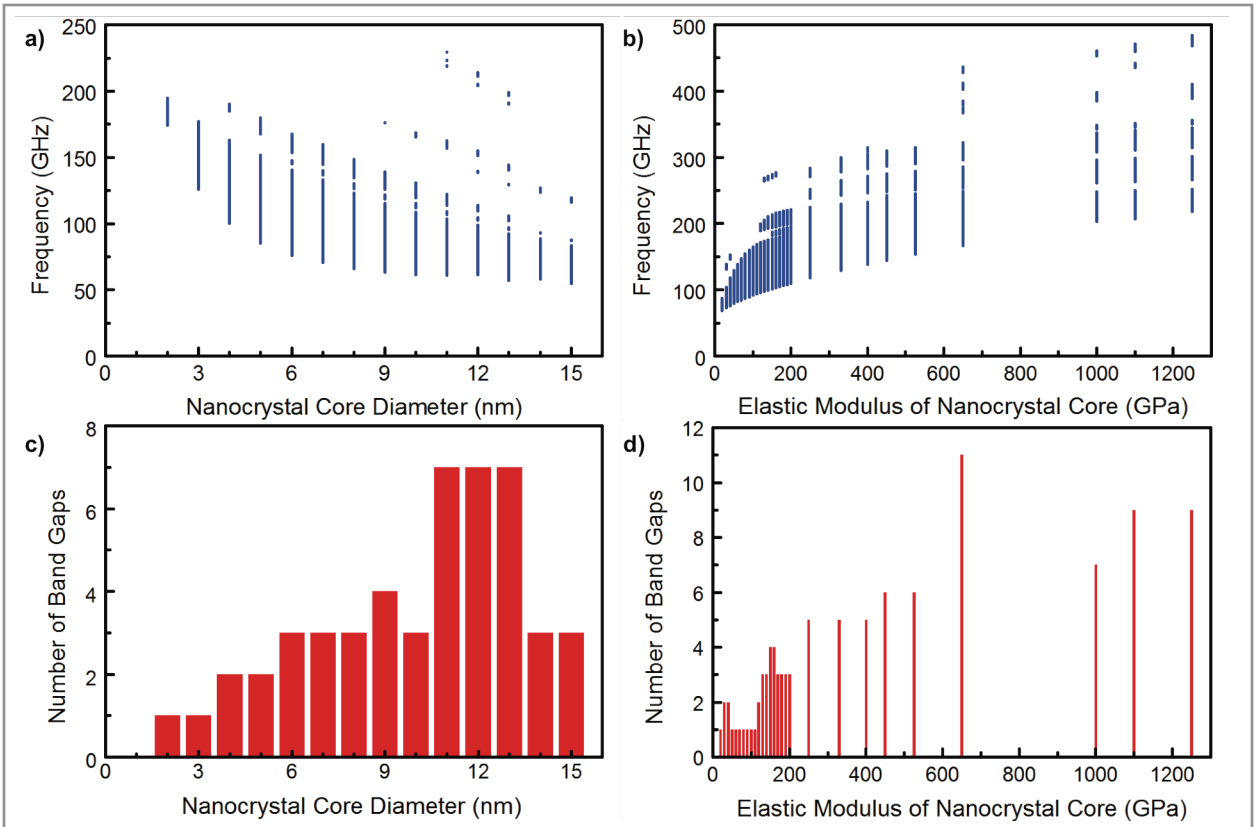

Figure 3.6. Frequency maps of the phononic band gaps in colloidal nanocrystal superlattices as a function of (a) nanocrystal core diameter and (b) nanocrystal core elastic modulus. The number of band gaps corresponding to each diameter and elastic modulus are shown in parts (c) and (d), respectively. Band gaps narrower than 5 GHz are not shown in these graphs. For diagram (a), the interparticle distance, ligand modulus, and nanocrystal core modulus are 1.5 nm, 1 GPa, and 54 GPa, respectively. For diagram (b), the interparticle distance, nanocrystal core diameter, and ligand modulus are 1.5 nm, 9 nm, and 2.6 GPa, respectively.

Another notable effect of changing nanocrystal core diameter and elastic modulus on the phonon band diagram is a re-scaling of the frequencies. While this frequency re-scaling leads to meaningful changes in the phonon band structure, its effects on the number of observed band gaps are artificial in nature. When downshifting the frequencies, one effect is the appearance of seemingly more phonon branches. However this apparent effect originates from our maximum frequency limitation of 500 GHz due to the continuum nature of our PWE model. These "new branches" are simply shifting from frequencies above 500 GHz to frequencies below 500 GHz. Another effect of this frequency re-scaling is the potential to flatten bands as the frequencies are downscaled. While one might assume that this frequency re-scaling could be the origin of band flattening described in the above paragraph, it should be noted that band flattening due to frequency re-scaling and band flattening due to property mismatches are independent effects. This is evident when inspecting Figure 3.7f, which simultaneously has the flattest optical bands and the least frequency downscaling.

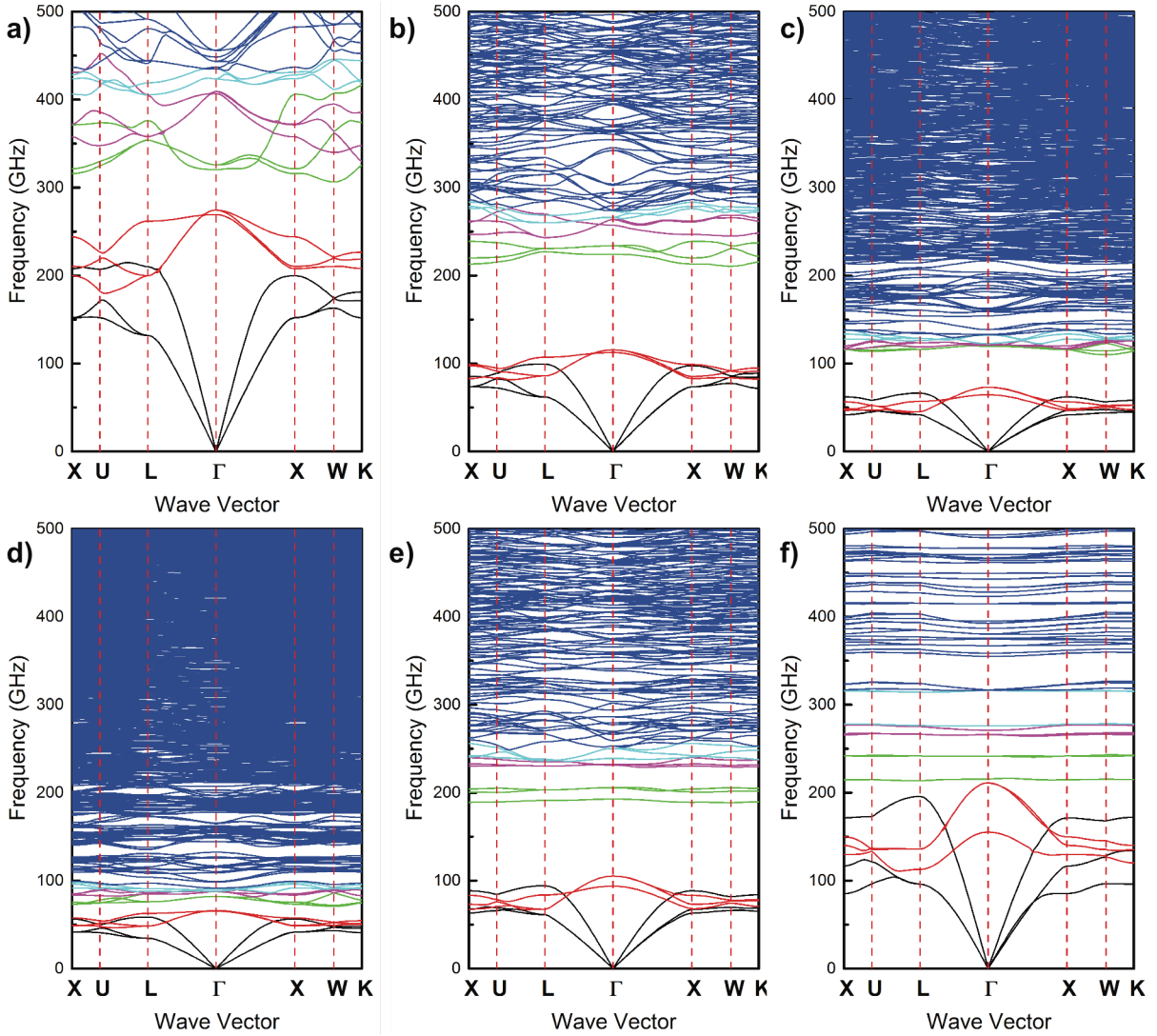

Figure 3.7. Phononic band diagrams for varying nanocrystal core diameters: (a) 2 nm, (b) 6 nm, and (c) 15 nm, and varying nanocrystal core elastic moduli: (d) 10 GPa, (e) 150 GPa, and (f) 1250 GPa. For diagrams (a) – (c), the interparticle distance, ligand modulus, and nanocrystal core modulus are 1.5 nm, 1 GPa, and 54 GPa, respectively. For diagrams (d) – (f), the interparticle distance, nanocrystal core diameter, and ligand modulus are 1.5 nm, 9 nm, and 2.6 GPa, respectively. To improve clarity, the first 5 sets of branches (i.e., 15 branches) are color-coded in each diagram. The three acoustic branches are black, the first set of optical branches are red, the second set of optical branches are green, and subsequent sets of optical branches are purple and cyan, respectively.

3.4. Conclusions

The results in this work illustrate that colloidal nanocrystals are excellent candidates for the bottom-up assembly of 3-dimensional phononic crystals. The nanoscale periodicity and acoustic contrast between the hard nanocrystal cores and soft ligand matrix lead to phononic band gaps with center frequencies on the order of ~ 10^2 GHz and band gap widths on the order of ~ 10^1 GHz. In addition, these characteristics can be tuned by changing the nanocrystal core diameter, nanocrystal core elastic modulus, interparticle distance, and ligand modulus. These results suggest that colloidal nanocrystal superlattices are promising candidates for use in high frequency phononic crystal applications that exert control over sound and heat.

3.5. Section 3 References.

1. M. Maldovan, *Nature*, 2013, **503**, 209-217.
2. T. Gorishnyy, M. Maldovan, C. Ullal and E. Thomas, *Phys. World*, 2005, **18**, 24-29.
3. M.-H. Lu, L. Feng and Y.-F. Chen, *Materials Today*, 2009, **12**, 34-42.
4. R. Olsson Iii and I. El-Kady, *Measurement Science and Technology*, 2009, **20**, 012002.
5. Y. Pennec, J. O. Vasseur, B. Djafari-Rouhani, L. Dobrzyński and P. A. Deymier, *Surface Science Reports*, 2010, **65**, 229-291.
6. M. M. Hossain and M. Gu, *Laser & Photonics Reviews*, 2014, **8**, 233-249.
7. S. John, *Physical Review Letters*, 1987, **58**, 2486-2489.
8. H. Chen and C. T. Chan, *Journal of Physics D: Applied Physics*, 2010, **43**, 113001.
9. R. H. O. III and I. El-Kady, *Measurement Science and Technology*, 2009, **20**, 012002.
10. A. Khelif, A. Choujaa, B. Djafari-Rouhani, M. Wilm, S. Ballandras and V. Laude, *Physical Review B*, 2003, **68**, 214301.
11. J.-H. Sun and T.-T. Wu, *Physical Review B*, 2005, **71**, 174303.
12. S. Yang, J. H. Page, Z. Liu, M. L. Cowan, C. T. Chan and P. Sheng, *Physical Review Letters*, 2004, **93**, 024301.
13. N. Boechler, G. Theocharis and C. Daraio, *Nat Mater*, 2011, **10**, 665-668.
14. M. Maldovan, *Physical Review Letters*, 2013, **110**, 025902.
15. R. Martinez-Sala, J. Sancho, J. V. Sanchez, V. Gomez, J. Llinares and F. Meseguer, *Nature*, 1995, **378**, 241-241.
16. F. R. Montero de Espinosa, E. Jiménez and M. Torres, *Physical Review Letters*, 1998, **80**, 1208-1211.
17. T. Gorishnyy, C. Ullal, M. Maldovan, G. Fytas and E. Thomas, *Physical review letters*, 2005, **94**, 115501.
18. S. Alaie, D. F. Goettler, M. Su, Z. C. Leseman, C. M. Reinke and I. El-Kady, *Nat Commun*, 2015, **6,** 7228.
19. N. Zen, T. A. Puurtinen, T. J. Isotalo, S. Chaudhuri and I. J. Maasilta, *Nat Commun*, 2014, **5,** 3435.
20. H. Shin, J. A. Cox, R. Jarecki, A. Starbuck, Z. Wang and P. T. Rakich, *Nat Commun*, 2015, **6,** 6427.
21. J. Gomis-Bresco, D. Navarro-Urrios, M. Oudich, S. El-Jallal, A. Griol, D. Puerto, E. Chavez, Y. Pennec, B. Djafari-Rouhani, F. Alzina, A. Martínez and C. M. S. Torres, *Nat Commun*, 2014, **5,** 4452.
22. A. Fainstein, N. D. Lanzillotti-Kimura, B. Jusserand and B. Perrin, *Physical Review Letters*, 2013, **110**, 037403.
23. M. Eichenfield, J. Chan, R. M. Camacho, K. J. Vahala and O. Painter, *Nature*, 2009, **462**, 78-82.
24. V. Narayanamurti, H. L. Störmer, M. A. Chin, A. C. Gossard and W. Wiegmann, *Physical Review Letters*, 1979, **43**, 2012-2016.
25. O. Koblinger, J. Mebert, E. Dittrich, S. Döttinger, W. Eisenmenger, P. V. Santos and L. Ley, *Physical Review B*, 1987, **35**, 9372-9375.
26. W. Cheng, J. Wang, U. Jonas, G. Fytas and N. Stefanou, *Nat Mater*, 2006, **5**, 830-836.

27. E. Alonso-Redondo, M. Schmitt, Z. Urbach, C. M. Hui, R. Sainidou, P. Rembert, K. Matyjaszewski, M. R. Bockstaller and G. Fytas, *Nat Commun*, 2015, **6,** 8309.
28. C. B. Murray, C. Kagan and M. Bawendi, *Annual Review of Materials Science*, 2000, **30**, 545-610.
29. J. Park, J. Joo, S. G. Kwon, Y. Jang and T. Hyeon, *Angewandte Chemie International Edition*, 2007, **46**, 4630-4660.
30. Y. Xia, Y. Xiong, B. Lim and S. E. Skrabalak, *Angewandte Chemie International Edition*, 2009, **48**, 60-103.
31. M. V. Kovalenko, L. Manna, A. Cabot, Z. Hens, D. V. Talapin, C. R. Kagan, V. I. Klimov, A. L. Rogach, P. Reiss, D. J. Milliron, P. Guyot-Sionnnest, G. Konstantatos, W. J. Parak, T. Hyeon, B. A. Korgel, C. B. Murray and W. Heiss, *ACS Nano*, 2015, **9**, 1012-1057.
32. S. A. Mcdonald, G. Konstantatos, S. Zhang, P. W. Cyr, E. J. Klem, L. Levina and E. H. Sargent, *Nature materials*, 2005, **4**, 138-142.
33. C.-H. M. Chuang, P. R. Brown, V. Bulović and M. G. Bawendi, *Nature materials*, 2014, **13**, 796.
34. X. Dai, Z. Zhang, Y. Jin, Y. Niu, H. Cao, X. Liang, L. Chen, J. Wang and X. Peng, *Nature*, 2014, **515**, 96-99.
35. K.-S. Cho, E. K. Lee, W.-J. Joo, E. Jang, T.-H. Kim, S. J. Lee, S.-J. Kwon, J. Y. Han, B.-K. Kim and B. L. Choi, *Nature Photonics*, 2009, **3**, 341-345.
36. R. Y. Wang, J. P. Feser, J.-S. Lee, D. V. Talapin, R. Segalman and A. Majumdar, *Nano letters*, 2008, **8**, 2283-2288.
37. F.-J. Fan, B. Yu, Y.-X. Wang, Y.-L. Zhu, X.-J. Liu, S.-H. Yu and Z. Ren, *Journal of the American Chemical Society*, 2011, **133**, 15910-15913.
38. F. J. Fan, Y. X. Wang, X. J. Liu, L. Wu and S. H. Yu, *Advanced Materials*, 2012, **24**, 6158-6163.
39. M. Liu and R. Y. Wang, *Scientific reports*, 2015, **5,** 16353.
40. M. Liu and R. Y. Wang, *Nanoscale*, 2013, **5**, 7234-7237.
41. M. Liu, Y. Ma, H. Wu and R. Y. Wang, *ACS Nano*, 2015, **9**, 1341-1351.
42. S. J. Oh, Z. Wang, N. E. Berry, J.-H. Choi, T. Zhao, E. A. Gaulding, T. Paik, Y. Lai, C. B. Murray and C. R. Kagan, *Nano letters*, 2014, **14**, 6210-6216.
43. M. E. Turk, J.-H. Choi, S. J. Oh, A. T. Fafarman, B. T. Diroll, C. B. Murray, C. R. Kagan and J. M. Kikkawa, *Nano letters*, 2014, **14**, 5948-5952.
44. M. B. Zanjani and J. R. Lukes, *Journal of Applied Physics*, 2014, **115**, 143515.
45. M. B. Zanjani and J. R. Lukes, *The Journal of Physical Chemistry C*, 2015, **119**, 16889-16896.
46. E. Shevchenko, D. Talapin, A. Kornowski, F. Wiekhorst, J. Kotzler, M. Haase, A. Rogach and H. Weller, *Advanced Materials*, 2002, **14**, 287.
47. D. V. Talapin, E. V. Shevchenko, A. Kornowski, N. Gaponik, M. Haase, A. L. Rogach and H. Weller, *Advanced Materials*, 2001, **13**, 1868.
48. N. Aravantinos-Zafiris and M. Sigalas, *Journal of Vibration and Acoustics*, 2013, **135**, 041003.
49. J.-H. Sun and T.-T. Wu, *Physical Review B*, 2007, **76**, 104304.
50. P.-F. Hsieh, T.-T. Wu and J.-H. Sun, *Ultrasonics, Ferroelectrics, and Frequency Control, IEEE Transactions on*, 2006, **53**, 148-158.
51. P. Jiang, X.-P. Wang, T.-N. Chen and J. Zhu, *Journal of Applied Physics*, 2015, **117**, 154301.
52. B. Graczykowski, M. Sledzinska, F. Alzina, J. Gomis-Bresco, J. S. Reparaz, M. R. Wagner and C. M. Sotomayor Torres, *Physical Review B*, 2015, **91**, 075414.
53. E. N. Economou and M. Sigalas, *The Journal of the Acoustical Society of America*, 1994, **95**, 1734-1740.
54. M. Kafesaki, M. M. Sigalas and E. N. Economou, *Solid State Communications*, 1995, **96**, 285-289.
55. M. S. Kushwaha, P. Halevi, L. Dobrzynski and B. Djafari-Rouhani, *Physical Review Letters*, 1993, **71**, 2022-2025.
56. R. Meyer, *arXiv preprint arXiv:1511.00739*, 2015.
57. J.-W. Jiang, *Nanoscale*, 2014, **6**, 8326-8333.
58. D. Sjöberg, C. Engström, G. Kristensson, D. J. Wall and N. Wellander, *Multiscale Modeling & Simulation*, 2005, **4**, 149-171.

59. H. Ibach, H. Lüth, L. Mihaly and D. Mandrus, *American Journal of Physics*, 1992, **60**, 1053-1054.
60. K. Bian, W. Bassett, Z. Wang and T. Hanrath, *The Journal of Physical Chemistry Letters*, 2014, **5**, 3688-3693.
61. P. Podsiadlo, G. Krylova, B. Lee, K. Critchley, D. J. Gosztola, D. V. Talapin, P. D. Ashby and E. V. Shevchenko, *Journal of the American Chemical Society*, 2010, **132**, 8953-8960.
62. P. Podsiadlo, B. Lee, V. B. Prakapenka, G. V. Krylova, R. D. Schaller, A. Demortière and E. V. Shevchenko, *Nano Letters*, 2011, **11**, 579-588.
63. R. G. Budynas, *Advanced strength and applied stress analysis*, McGraw-Hill Science/Engineering/Math, 1998.
64. D. Cheney, 2013.
65. D. A. Cheney and J. R. Lukes, *Journal of Heat Transfer*, 2013, **135**, 091101.
66. G. Taras, M. Martin, U. Chaitanya and T. Edwin, *Physics World*, 2005, **18**, 24.
67. N. W. Ashcroft and N. D. Mermin, *Appendix N*, 2010.